

# Space Launch System Core Stage Green Run Base

## Heating: Anomaly, Mitigation and Flight Redesign

Manish Mehta<sup>1\*</sup>, Christopher I. Morris<sup>1&</sup>, Brandon L. Mobley<sup>1#</sup> and Terry L. Prickett<sup>1+</sup>

*NASA Marshall Space Flight Center, Huntsville, Alabama 35812*

The NASA Space Launch System (SLS) vehicle is composed of four RS-25 liquid oxygen and hydrogen rocket engines in the Core Stage (CS). The SLS Core Stage went through Green Run hot-fire testing at NASA Stennis Space Center's B-2 test facility in 2021. The main goal of this testing was to confirm Core Stage tanking, propulsion and thrust vector control systems operations and performance to verify with predicted models. Two hot-fire (HF) test sequences were performed with the first one (HF1) in January for a test duration of 70 seconds and the second (HF2) testing completed in March for a test duration of 500 seconds. This paper focuses on the base heating anomalies observed during HF1 and HF2 where an extensive fire was observed along the Core Stage base heat shield during test operations. This environment was not anticipated and led to extensive unplanned damage to the thermal protection system which was augmented for flight. Green Run observations also led to a reassessment of flight environments for Artemis I. This paper discusses the potential cause of the anomalies, the flow physics, the reconstructed base environments, and mitigation plans for HF2 and flight.

---

\* Subject Matter Expert, Aerothermodynamics, Aerosciences Branch, Senior Member AIAA

& Branch Chief, Aerosciences Branch, Senior Member AIAA

# Aerothermodynamics Team Lead, Aerosciences Branch, Senior Member AIAA

+ Stages Deputy Chief Engineer, Chief Engineer Office, Member AIAA

## Nomenclature

$A$	=	surface area
AF	=	air-to-fuel ratio
BHS	=	base heat shield
BT	=	boat-tail
CFD	=	computational fluid dynamics
CS	=	SLS core-stage
CAPU	=	Core Auxiliary Power Unit
$d$	=	flame diameter
DFI	=	Development Flight Instrumentation
E	=	RS-25 engine
EMHS	=	Engine-Mounted Heat Shield
FLT	=	flight condition
GR	=	Green Run
$GH_2$	=	gaseous hydrogen
HF1	=	Hot-Fire 1
HF2	=	Hot-Fire 2
AR01	=	Artemis I Flight
$h$	=	specific enthalpy
$k$	=	gas thermal conductivity
$L$	=	flame length
$Ma$	=	Mach number
$Nu$	=	Nusselt number
$\dot{m}$	=	mass flow rate
O/F	=	oxidizer to fuel mass flow rate ratio
$P$	=	pressure
PGR	=	Post-Green Run

$Pr$	=	Prandtl number
$Q$	=	total heat load
$\dot{q}$	=	heating rate
$R$	=	gas constant
$Re$	=	Reynolds number
$HBOI$	=	hydrogen burn-off igniters
$S$	=	maximum laminar burning velocity
$SLS$	=	Space Launch System
$SRB$	=	Solid Rocket Booster
$SSC$	=	Stennis Space Center
$\tau$	=	wall shear stress
$T$	=	temperature
$t$	=	time
$U$	=	velocity
$TVC$	=	thrust vector control
$TPS$	=	thermal protection system
$X$	=	axial distance
$\gamma$	=	specific heat ratio
$\rho$	=	gas density
$\mu$	=	gas viscosity
$\sigma$	=	one standard deviation

#### Subscripts

$0$	=	non-coaxial flame, stagnation point
$a$	=	air
$B0$	=	blow off
$c$	=	convection
$f$	=	flame, fuel
$FLT$	=	flight condition

$G$	=	gauge
$J$	=	jet
$1,2,3,4$	=	RS-25 engine number
$r$	=	radiation
$rec$	=	recovery
$T$	=	total
$temp$	=	temporal
$w$	=	wall

## I. Introduction

### A. Background

The NASA Marshall Space Flight Center (MSFC) Aerosciences Branch is responsible for developing ascent plume induced thermal design environments for the Space Launch System (SLS) vehicle. The exhaust plume environments contain both radiation and convection modes of heat transfer. The dominant heat source early in flight is radiation from the solid rocket motor plumes and to a lesser extent from the RS-25 engine hydrogen – oxygen plumes. Early in flight, vehicle base components experience convective cooling due to the aspirating nature of the plumes [1-3]. Later in flight, as altitude increases, and pressure decreases, the plumes expand and begin to interact with each other resulting in reverse flow of hot gases into the base. It is at high altitude where significant plume interaction occurs that the base elements experience peak convective heat flux [1-3]. After Booster separation, the core-stage (CS) experiences a lower level convective heat flux for a longer period of time [2]. In summary, boost phase flight experiences peak convective heat flux, while the core-only phase experiences the largest time integrated convective heat load. Due to the complex nature of plume-induced base flows, wind tunnel testing has traditionally been pursued to lower uncertainty in these environments.

Base heating environments are one of the highest design risks for a launch vehicle due to the lack of analytical solutions to adequately predict base flow behavior and the highest heating environments historically observed during launch vehicle ascent [4]. The base region of a launch vehicle has multiple

rocket engines clustered to provide the needed thrust (Figure 1). Multiple rocket plumes and plume-freestream air interactions lead to complex flow field and high heating environments. Multi-rocket engine launch vehicles are common and have been used historically in the Shuttle, Saturn V and Saturn IB vehicles and as well as the new Space Launch System (SLS). The larger the thrust and the number of engines, the greater the complexity of the flow field and importance in accurately predicting base environments to capture all the high temperature regions. Accurately predicting base flow environments are critical for efficiently and safely designing thermal protection systems (TPS). A lack of understanding of launch vehicle base environments led to a series of anomalies and catastrophic rocket explosions from the 1960s to the 2000s. Inadequate predictions of base heating and flow physics have led to the failures of many government and private launch vehicles during ascent (e.g. Polaris, Atlas, N-1, Prospector, etc.) [4]. Hot rocket plume-induced base flows can lead to thermal breakdown of multiple components within the vehicle base such as the engine thermal boots, propulsion systems, gimbal actuators, cabling for avionics and structural hardware. Thermal protection systems (TPS) are used to protect these components from high heating environments and degradation and their design can be compromised and lead to mission failure due to inadequate environment predictions and TPS design. On the other hand, overly conservative TPS design, which can weigh ~2,000 lbs on the base heat shield and engine compartment and an additional ~2,000 lbs for the engine close-outs and other supporting brackets for a typical launch vehicle, can lead to a reduction in payload mass. One pound reduction in TPS mass leads to increase in payload mass which is dependent on the gear ratio. This initial Block I version of SLS, with four RS-25 engines and two solid rocket boosters, will generate 8.8 million lbf of thrust at lift-off, larger than the 7.9 million lbf generated by Saturn V. As a result, base heating rates and drag are expected to be significant and the flow physics needs to be understood for efficient and safe design of the thermal protection system (TPS).

The main motivation of this paper is to investigate the base flow physics at SLS flight-scales during the Core Stage Green Run (GR) test campaign. Up to this point, all base environments were developed through a 2% sub-scale propulsion model in a shock tube [4], Shuttle-derived flight data [2] and computational simulations [5]. There were still many base heating unknowns as to the effects of RS-25 radiation within the test stand, the Core Auxiliary Power Unit (CAPU) hydrogen burning plumes which

were modeled using computational simulations and the effect of scale. The Green Run tests provided a valuable opportunity to observe flight-scale base flow behavior at sea-level conditions.

The Core Stage is composed of multiple elements as shown in Figure 1. At the top of the Stage is the forward skirt, followed by the liquid oxygen (LOX) tank, intertank, liquid hydrogen (LH<sub>2</sub>) tank and the engine section. The engine section is one of the most complex elements of the vehicle as it houses all the avionics and thrust vector control (TVC) for the four RS-25 engines. The Core Stage is one of the newest elements of the SLS vehicle compared to elements derived from the Space Shuttle Program. As the Core Stage is the backbone of the SLS vehicle (Figure 1), on either side are attached the 5-segment solid rocket booster (SRB) and on-top is the Launch Vehicle Stage Adapter (LVSA), Intermediate Cryogenic Propulsion Stage (ICPS) and the Orion Stage Adapter. On top of the in-space stage is the Orion spacecraft and Launch Abort System (LAS). This complex system outputs 2 million pounds of vacuum thrust at lift-off from the Core Stage and 6.8 million pounds of vacuum thrust from the two 5-segment SRBs at lift-off.

There are various base components for the vehicle that are instrumental for mission success. The base heat shield (BHS) protects the base of the Core Stage and its' internal components from excessive heating. Cork is being used for the BHS TPS material for the first several flights of the SLS vehicle. The BHS and boat-tail (BT) encompasses approximately 481 square feet of area. The engine-mounted heat shield (EMHS) protects RS-25 turbopump machinery and gimbal actuators. Total EMHS coverage is 440 square feet. A thermal blanket is being used for the EMHS and this is described in more detail in later sections. There are other important base components that are sensitive to high heating rates and loads such as the BT, the booster separation motors (BSM), the SRB aft-skirt and the aft attach struts as shown in Figure 1. The RS-25 and RSRMV nozzles are also sensitive to plume induced heating. These loads may have an effect on the RSRMV liner to housing adhesive bondline. The excessive heating areas of concern for the RS-25 nozzles are the hat-bands, drain lines, fuel transfer ducts and support brackets. These components need to be within the appropriate substrate temperature range during the vehicle flight to prevent catastrophic failure. As a result, heating rates and heat load need to be accurately predicted to appropriately design the TPS for these components.

As outlined above, the base of the Core stage is also composed of four critical components: (1) angled boat-tail; (2) base heat shield; (3) RS-25 engine blankets; (4) four RS-25 engines. The first three

components provide thermal protection to the Stage and the engines during ascent. The base heat shield is 28.3 feet in diameter and is flat in contour as shown in Figure 2. There is a central access port which is termed the manhole cover (Figure 2) that is sealed up prior to launch and hot-fire testing. The base heat shield comes in multiple sheets of the P50 cork ablator, shown in brown color in the left panel of Figure 2. There are small, localized brick cut-outs within the base heat shield where the RT455 ablator is sprayed on in regions where there are gaps and protruding bolts. The P50 cork ablator is applied by an adhesive to a thin membrane metal substrate. The P50 cork ablator has white Hypalon top coating for protection against mold/fungi and UV exposure, not shown in Figure 2. Figure 3 shows the Core Stage at NASA Stennis Space Center (SSC), integrated with the B-2 test stand. The entire base heat shield and boat tail are covered with reflective foil with an emissivity of 0.1 (right panel of Figure 2) to minimize the radiative environments on the heat shield. This was done to keep the ablator as pristine as possible during hot-fire testing. The goal for the Green Run hot-fire test campaign was to conduct minimal refurbishment of the heat shield prior to delivery to NASA Kennedy Space Center. Reflective foil was shown at a MSFC Hot-Gas Facility and Thermal Vacuum Chamber test campaign to survive Green Run radiation heat loads and to minimally impact the ablator or the reflective foil.

The Core Stage Green Run test campaign involved verifying: (1) the 700,000 gallons of LH<sub>2</sub> and LOX tanking approaches (termed “Wet Dress Rehearsal”), (2) the thrust vector control systems and operations, (3) Stage avionics system, (4) the preconditioning the RS-25 engines prior to ignition, (5) the modal response of the integrated Stage, (6) countdown operations and (7) full-duration 500-sec hot-fire test of the four RS-25 engines, following a similar flight profile. Another unique aspect about this test program was that the Core Stage was not only a ground test article but also a flight test article. This incurred additional scrutiny in the test approaches and updates to test protocols previously developed for the Space Shuttle Main Propulsion Test Article (MPTA) [6]. The SLS Green Run test campaign was conducted at the NASA Stennis Space Center B-2 Test Stand from mid-2020 to mid-2021. There is one flame trench for all four RS-25 engine plumes and it has an active deluge system during engine operation. The Green Run test campaign was not conducted to validate the Stage induced aerothermal environments prior to flight. However, there was a decision by the SLS Program to keep all the Developmental Flight Instrumentation (DFI) active during hot-fire test operations.

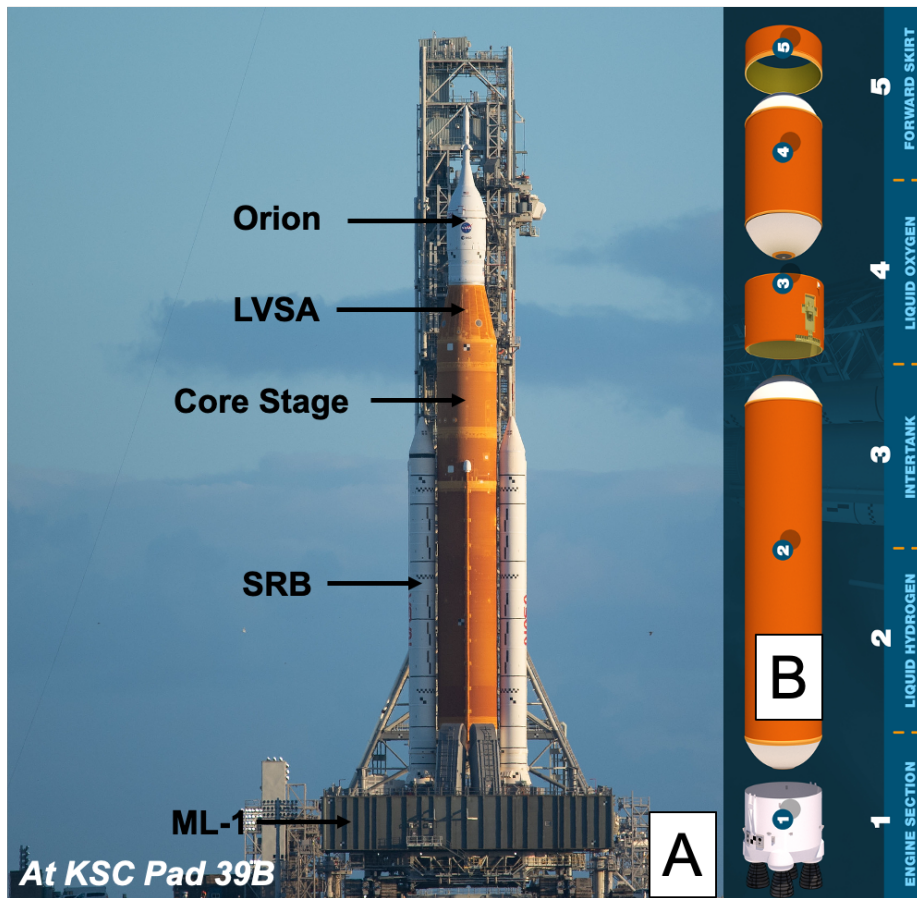


Figure 1. (a) SLS Vehicle; (b) Core Stage

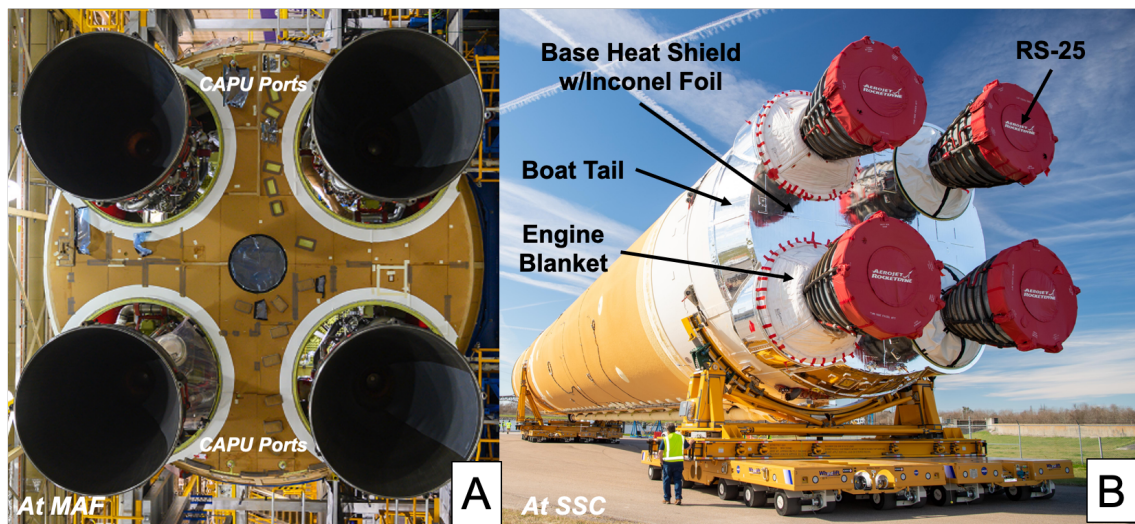
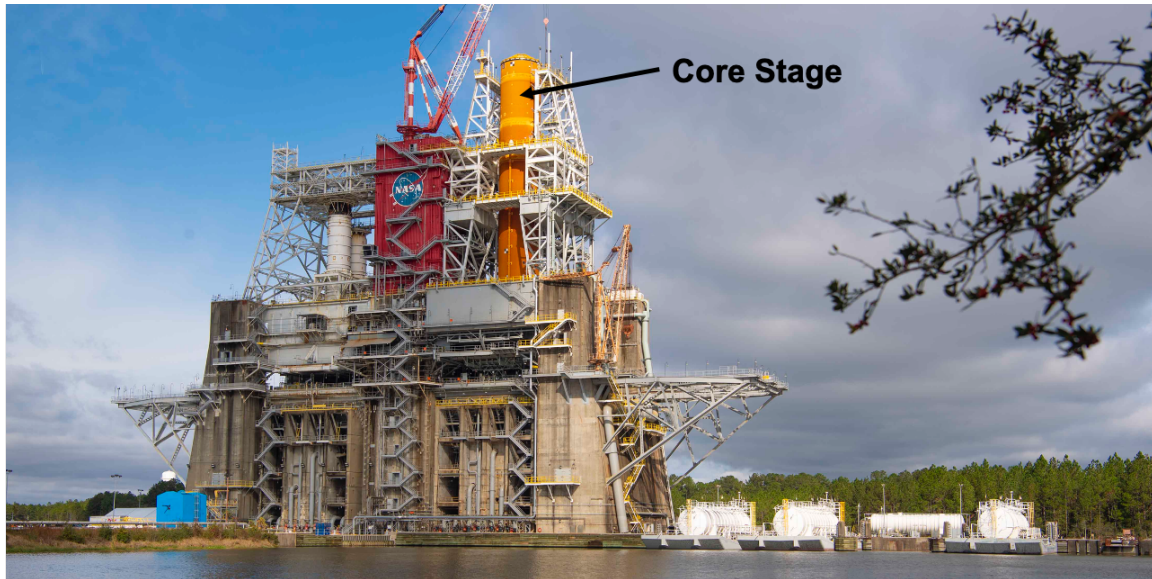


Figure 2. (a) Applying the Core Stage base heat shield at MAF; (b) Core Stage base region at SSC



**Figure 3. Core Stage within the NASA SSC B-2 test stand in preparation for the Green Run Testing**

## **II. Green Run Hot-Fire 1 (HF1) Base Heating Anomaly**

### **A. Core Stage Base Heat Shield Developmental Flight Instrumentation (DFI)**

There was DFI on the base heat shield as laid out by NASA and Boeing early in the Core Stage development phase. Since the BHS was initially predicted to have the largest ascent aerothermal heat loads on the Stage and with considerable uncertainty in prediction, a large number of heat transfer and pressure sensors was applied on the base heat shield. There were 45 sensors on the base heat shield and boat tail that would provide heat transfer data. There are a total of 4 different type of sensors that provide the needed heat transfer data to correlate to the base heating models. This is comprised of a Schmidtt-Bolter calorimeter which outputs incident total heat flux with a calorimeter housing Type-K thermocouple to provide a reference temperature (Figure 4) [6-8]. The second type of instrumentation is a Schmidtt-Bolter radiometer which outputs incident radiative heat flux within the visible and infrared wavelength bands (Figure 4). There is a Sapphire window over the sensor head which

provides ideal transmissivity within the visible and infrared and prevents artificial readings from convective heat transfer. The third type is a gas temperature probe (GTP) which has a protective shielding and perforated holes to provide accurate gas temperature measurements. The protective shielding is to minimize thermocouple damage due to debris and excessive radiation. The fourth type is a static surface pressure transducer (Kulite) which provides surface pressure measurements. The pressure gauge provided a dual-purpose in assessing heat transfer and base pressure. All the heat transfer and pressure sensors are provided by MEDTHERM and Kulite which have extensive Shuttle heritage [7-9].

There are 8 aerothermal DFI islands arranged in a cross pattern along the base heat shield and there is one DFI island suite on the boat tail and two on the engine fairing (Figure 4). Identification numbers are shown in bold next to each DFI island and will be referenced throughout this paper. As can be seen in Figure 4, the calorimeter, radiometer, and pressure sensor are all flush within +/- 0.005 inches with the TPS on the base heat shield based on requirements. In some instances, the radiometer was slightly recessed into the TPS and as a result local coning of the TPS was needed to minimize field of view obstruction. Both the calorimeter and radiometer have a 150-degree field of view (FOV) which minimizes the needed correction if the FOV were different between the two sensors [7]. The GTP sticks out from the base heat shield by 3 inches to measure the boundary layer gas temperature. The pressure transducer has a tube from the external OML orifice to the diaphragm head which is embedded forward of the heat shield. There was a goal to collocate sensors on an island to easily reconstruct base pressure, base force, convective heating, film heat transfer coefficient, and Reynolds Number exponent in turbulent flat plate theory assessments. Importantly these parameters would allow to adequately compare flight environments with predicted design environments. Further understanding of scaling sub-scale test data to flight could also be investigated. All of these DFI sensors were active for the GR HF1 test campaign.

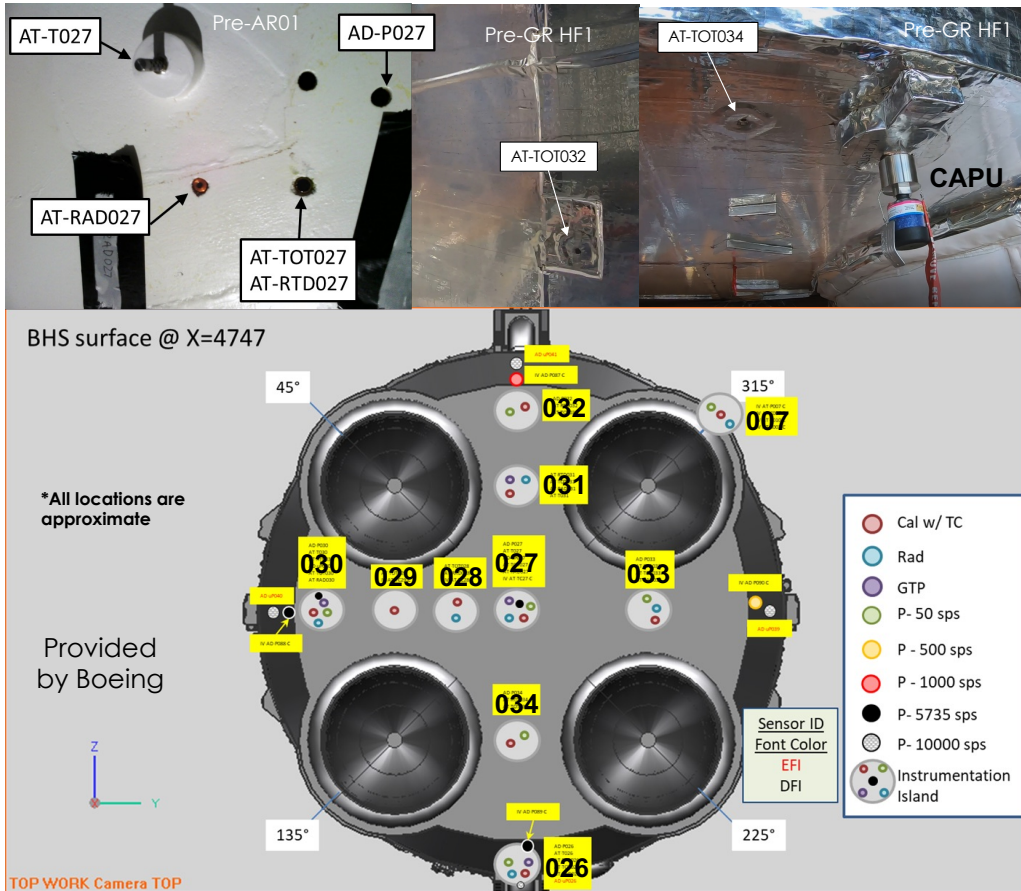


**Figure 4. (above)** Three figures show the base heat shield development flight instrumentation (DFI) embedded within the TPS for both pre-GR HF1 and pre-AR01; Reflective Nexolve tape can be seen covering the BHS TPS; **(bottom)** full Core Stage base heat shield DFI layout [7-9]

## B. GR HF1 Core Stage Base TPS Configuration

The Core Stage base was put in a GR TPS configuration to minimize refurbishment of the base secondary and primary structures. As described above, Nexolve reflective foil covered the entire base heat shield and boat-tail regions of the Stage to reduce incident radiation on the TPS and hardware. Underneath the foil, there was 1.0" thickness of Hypalon/P50 cork wedges applied near the CAPU exhausts and 0.7" thickness of Hypalon/P50 cork applied everywhere else on the heat shield. In areas where there were gaps in cork or bolt bulkheads, RT455, a cork spray-on derivative, was applied in the shape of bricks. This is shown as magenta rectangles in Figure 5. SOFI-180 foam was applied to seal the circular manhole cover, shown in yellow within Figure 5. This was the proposed base TPS configuration for flight with the

reflective foil and the SOFI-180 foam added specifically for the Green Run test campaign. Closeup pre-test pictures of the GR HF1 base configuration can be shown in Figure 6. Note the careful detail of application of the Nexolve reflective tape to the entire base heat shield and boat tail regions of the Stage. No reflective tape was applied on the RS-25 engine blankets, shown in white within Figure 6. However, rain shield barriers were applied to protect the thermal blankets from the natural elements. All the DFI islands were covered with foil, but the sensor heads were exposed to capture test data.

GR HF1 post-test images of the base region are shown in Figure 7. It can clearly be seen that a portion of the reflective foil, foil adhesive, Hypalon and P50 cork burned near the CAPU ports between Engine 1 (E1) and Engine 4 (E4). This anomaly first occurred due to burning of the tape adhesive and Hypalon paint followed by combustion of the base heat shield insulation which ensued at T+52 seconds into the test. The TPS burning ensued until the RS-25 engines shut-down at T+67.6 seconds. It can be seen that a large flame front on the heat shield was observed from visible imagery between E1 and E4 (shown as large bright orange flames in Figure 7). Prior to the large-scale TPS burning, it can be seen from the top-right panel of Figure 7 that the Nexolve foil and adhesive had caught on fire at T+18 seconds. Although not conclusive, it is believed that the Hydrogen Burn-Off Igniters (HBOIs) hot pyrotechnic particles impinged on the foil at the lip of the boat tail, resulting in foil degradation and delamination. This compounded by the air entrainment due to the RS25 plumes further increases suck-down forces leading to delamination if there was a air flow field path on the inner bond line of the tape. Once the aluminum tape and adhesive started burning, it is clear that delamination of the foil was observed. This large-scale fire on the heat shield was not anticipated by NASA or the Contractors and an anomaly Tiger Team was set up to resolve and/or mitigate this issue. Also, there was no Shuttle experience since such heat shield fire was not observed on the Orbiter MPTA static-fire test [6]. Since the orbiter had non-ablative tiles, this environment was not a concern for the Shuttle Green Run test campaign.

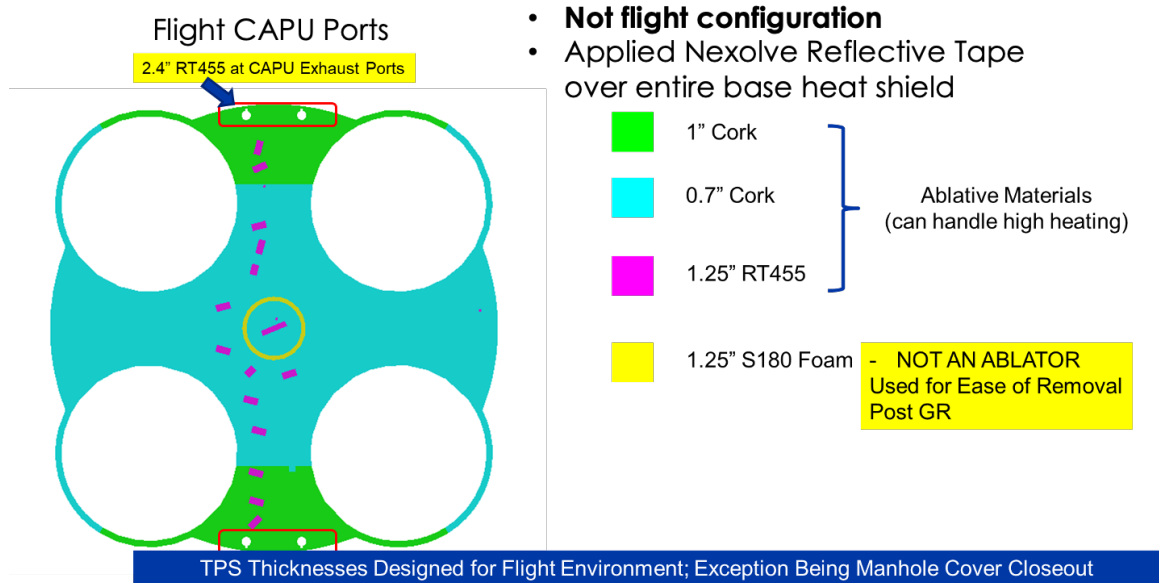


**Figure 5. Green Run Hot Fire 1 base TPS configuration**

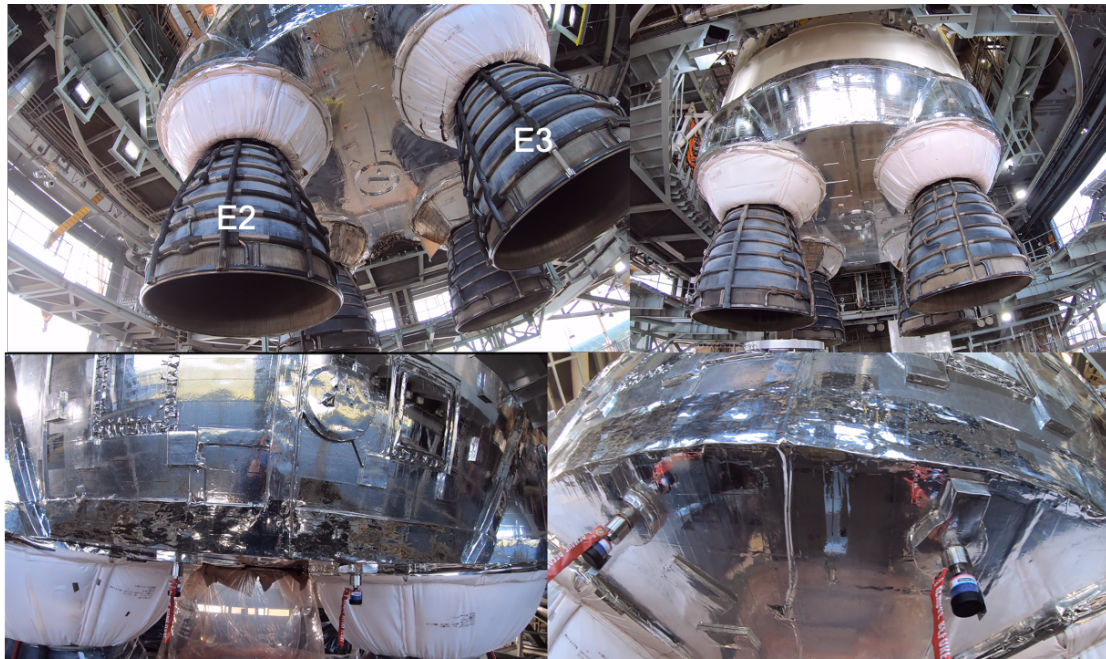


**Figure 6. Base heat shield, engine blanket and boat tail configurations at the SSC B-2 test stand prior to Green Run Hot Fire 1 test campaign**

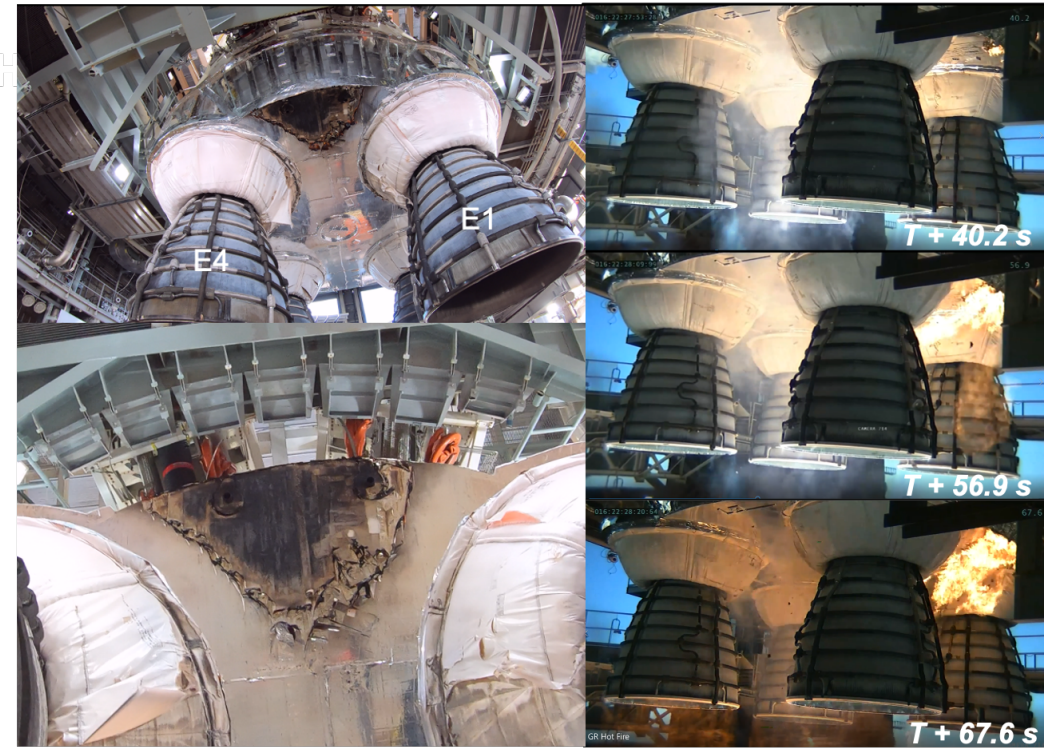


**Figure 7. (left) Base heat shield TPS damage during GR HF1; (right) Visible camera imagery of the Core Stage base during GR HF1 engine operation**

### C. GR HF1 Core Stage Base Aerothermodynamics Reconstruction

Reconstruction of GR HF1 base heat shield environments was pursued to fully understand the anomaly and potential mitigation paths moving forward. Several steps were employed to reconstruct the aerothermal environments. The first component, verification of a true T-0 time starts when an ignition command is sent to E1. The rest of the engines have a staggered transient start-up to minimize engine ignition over pressure. All the DFI are reduced with this T-0 time reference. A second component was time-syncing all the base aerothermal DFI through fine linear interpolation. This enabled accurately estimating the convective heat flux by subtracting the radiative heat flux from the total heat flux measurements (Equation 1). A third component was reducing the calorimeter, radiometer and pressure data using serial calibration files instead of using the generalized calibration files. Serial calibration uses the calibration coefficients specific to that sensor. This was observed to show a difference of +/- 10% between serial and general calibration approaches. A fourth component

was syncing up the camera visible (VIS) and infrared (IR) images to the DFI data to further visualize the base flow physics and the anomaly. The fifth component was applying a 1-D moving average filter to the base pressure data due to the significant noise in the raw data. The sixth component involved applying GR radiation model trends in conjunction with radiometer data in estimating the radiative heating in DFI islands where radiometer data does not exist. For instance, this approach was applied to 032, 029 and 034 islands. These reduction approaches were applied to all the DFI to fully understand the base heating environments during GR HF1.

After the reconstruction was complete, a radiative heat flux, convective heat flux and total heat flux distribution with respect to test time was developed for each of the islands on the base heat shield (shown in Figure 8). The 032 island showed the sole evidence of the aerothermal environment effects of a deflagration on the base heat shield. This region is closest to the CAPU ports between E1 and E4 and positioned where the foil adhesive and cork burning was observed. It can be observed that the convective heat transfer to the heat shield significantly increases during the cork TPS burning regime. This non-linear increase in convective heating occurs from T+52 seconds to RS-25 engine shutdown. After T+62 seconds, there was a data error in the Huntsville Operation Service Center (HOSC) processing which resulted in noisy data. However, the peaks of the data are credible and were used in anomaly assessments. Convective and radiative heating are relatively constant from HBOI shutdown to just prior to large-scale burning. There are larger peaks in the convective heat flux distribution than the radiative heating. It should be noted that there is a ramp up in convective heating observed during engine ignition, prior to main-stage, while in contrast to the radiative heating which reaches steady state values in less than 2 seconds. This is due to the fact that the RS25 Mach disc come into the base field of view shortly after engine start-up, leading to a jump in radiative heating environments.

Initial observation and in-depth study of P50 cork combustion was observed from Sakraker et al, 2020 which showed that high enthalpy plasma ( $T \sim 10,000$  K) impinging on cork can lead to TPS burning as observed in Figure 9. [10] Although this mechanism is considerably different than observed for GR, the general TPS thermochemistry that leads to cork combustion are the same. The mechanisms that can lead to large convective heat flux on the TPS and induce ablation are: (1) pyrolytic gas burning with the freestream oxygen; (2) oxidation of the alpha-char which releases considerable

energy and imparts a large convective heat flux on the surface; (3) shear-induced high convective heating ablation which leads to the formation of fresh char layer and recession. Char oxidation releases 12,345 BTU/lbm of energy and leads to increases in the local gas temperature to 1800 deg R at STP [10-11].

The 031 island was also explored but did not exhibit the large rise in convective heating during the large-scale cork burning regime (Figure 10). However, there is a gradual rise in convective heating during test duration. It should be noted that the cork burned region as observed in Figure 7 occurred just outboard of this DFI island and so it did not measure cork TPS burning environments. Gas temperature data between E1 and E4 was also measured to show the highest temperature of all three gas temperature probes. Cork burning flames resulted in a hot boundary layer gas, where the gas temperature measurement at the base center and near the 030 island showed very modest increase from the ambient.

The 034 island which is located between E2 and E3 near the CAPU ports showed an average negative convective heating for the full duration of the test (Figure 11). Here, there was convective cooling observed due to air entrainment caused by the RS-25 plumes acting as efficient ejectors. Basically, the high air entrainment of ambient temperature leads to convective cooling within this region. It should be kept in mind that the radiometer and calorimeter were not collocated, and a symmetric radiometer gauge was used (RAD031) was used for this assessment.

Figure 12 shows base environments in terms of convective heating and surface pressure. Between E2 and E3, air entrainment leads to negative pressure differential and convective cooling. Between E1 and E4, high convective heating and positive surface pressure differential are noted. This is the first sign that CAPU H<sub>2</sub> burning flames are affecting the base flow physics. It can be seen from the surface pressure plots that CAPU plume impingement on the base heat shield leads to positive pressure loads on the TPS and a positive base convection. Also, to note is that the large-scale fire regime resulted in a high surface pressure and high convective heating between E1 and E4 near the CAPU ports.

Figure 13 shows the average convective and radiative heating distribution as a function of radial distance from the base centerline along the CAPU and SRB lines. There is a comparison between nominal test window and the full-duration test. The nominal test window is after ROFI shutdown and

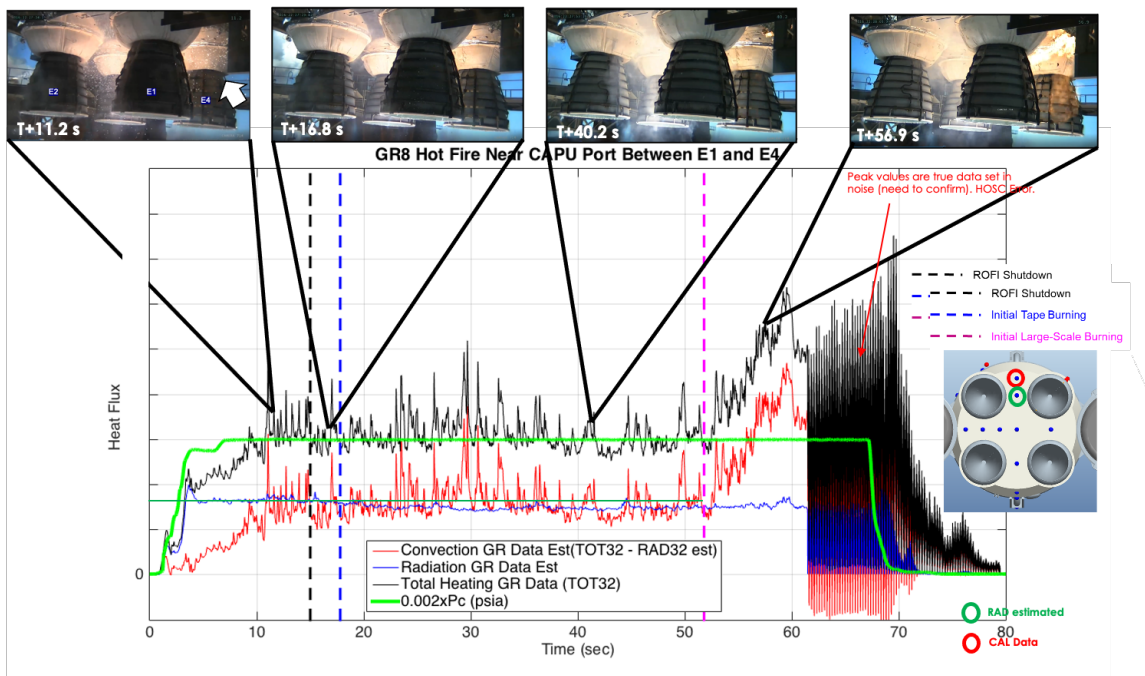
prior to first observation of Nexolve tape burning. It can be clearly seen that the convective heating increases as we get closer to the base TPS burning side, between E1 and E4. The radiative heating is somewhat like a Gaussian distribution along the CAPU line with peak radiative heating at the base center. The convective heating along the SRB line is positive and relatively flat.

Figure 14 shows the IR imagery of the CAPU H<sub>2</sub> plume dynamics during GR HF1. It can be seen that between E1 and E4, the H<sub>2</sub> burning plumes attach to the base heat shield during certain instances of operation. The CAPU H<sub>2</sub> has two flow states: high mass flow and low mass flow. During the low mass flow rates, the entrained air blows the H<sub>2</sub> burning plume toward the base center, resulting in the plume in attaching to the heat shield. During high mass flow rate, the H<sub>2</sub> plumes are directed downward away from the heat shield. Between E2 and E3, the H<sub>2</sub> burning plumes do not stagnate on the heat shield in the low flow state as the E1 and E4 region as observed in Figure 14. This is a result of high air entrainment which directs the H<sub>2</sub> plume downward and away from the heat shield. A working theory is that less air entrainment (lower velocity) on the E1 and E4 side due to test stand obstructions leads to a recirculation of the H<sub>2</sub> burning plume which enables easier flame reattachment on the heat shield. This leads to the IR imagery observation, augmented convective heating on that side and eventual cork burning. It should be noted that the measured HF1 nominal base convective heating was higher than predicted for Green Run environments for all the DFI islands. This base convective heating except 034 appears to be entirely due to CAPU H<sub>2</sub> burning exhaust effects.

Three-dimensional large-eddy simulation (LES) computational models provide further insight on the Green Run base flow physics [12]. These simulations were conducted for a low-altitude Mach 0.1 flight scenario but are considered qualitatively relevant for the Green Run. Figure 15 shows both instantaneous and average static gas temperature contour distribution within the base region for the low flow state CAPU operation. The localized base recirculation zone is developed by induced entrainment of air by the RS-25 plumes and the low flow-state CAPU H<sub>2</sub> burning flame attachment is driven by the plume cross-flow characteristics and its' low momentum flow state. This recirculation zone that is developed from the CAPU ports to the heat shield shows clear observation of CAPU H<sub>2</sub> plume attachment on the heat shield. There is qualitative good agreement between test data and computational simulations in showing the GR base flow environments.

To further validate the theory, Figure 16 shows that the B-2 test stand fixture around the Core Stage. It can be seen that there is more hardware between the Stage and B-2 test stand fixtures between the E1 and E4 region. The restricted clearance on the E1/E4 region constrains the entrained flow, leading to lower velocities and stronger potential of flow recirculation with the CAPU exhaust. It can be seen there is good air flow clearance in the E2/E3 region from Figure 16. This enables high flow entrainment and convective cooling as captured from the DFI heating and pressure data.

$$\dot{q}_c = \dot{q}_T - \dot{q}_r \quad (1)$$



**Figure 8. GR HF1 base heating environments near the CAPU ports between E1/E4. (top) base heat shield 032 total (black line) and radiative (blue line) heating data; overlaid with the RS-25 chamber pressure data (green line) and visual imagery during GR HF1; vertical dashed line = HBOI shutdown; vertical blue line = initial tape burning; vertical purple line = initial large-scale burning observation; right schematic showing the location of the DFI**

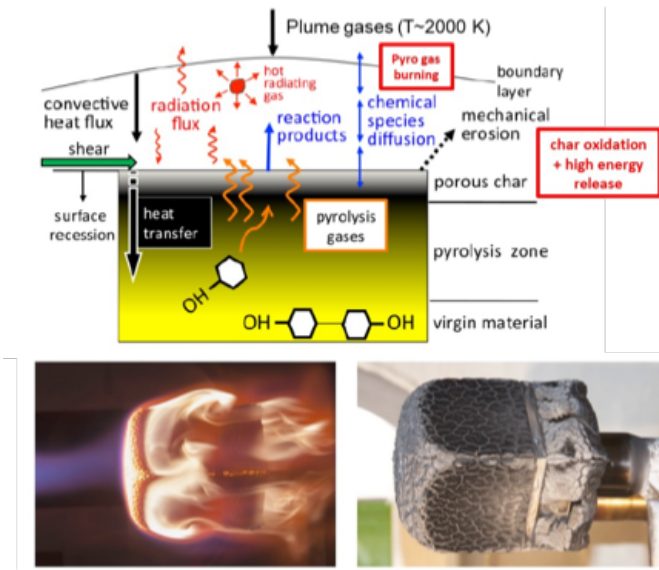


**Figure 9. (top)** schematic of TPS thermochemistry and ablation physics; major mechanisms are char oxidation, pyrolytic gas burning and shear-induced ablation; **(bottom)** *Sakraker et al, 2021, P50 cork burning and post-test observation due to high energy plasma flow within the Plasmatron [10]*

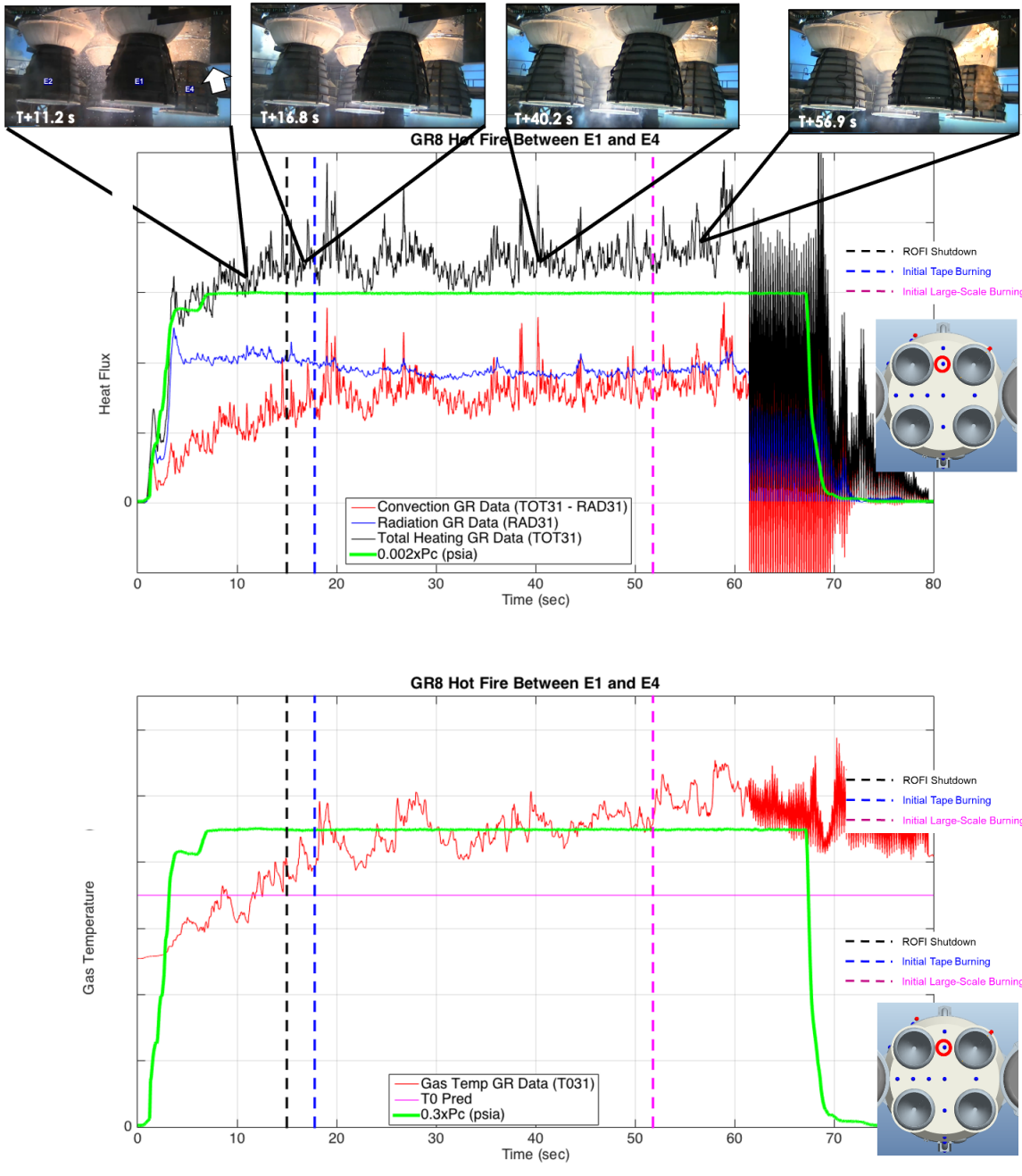


**Figure 10. (top)** base heat shield 031 total (black line) and radiative (blue line) heating data; overlaid with the RS-25 chamber pressure data (green line) and visual imagery data during GR HF1; vertical dashed line = HBOI shutdown; vertical blue line = initial tape burning; vertical purple line = initial large-scale burning observation (bottom) base heat shield 031 gas temperature data; overlaid with the RS-25 chamber pressure data (green line); White arrow shows approximate location of the DFI being assessed; base heat shield schematic shows location of the DFI being assessed

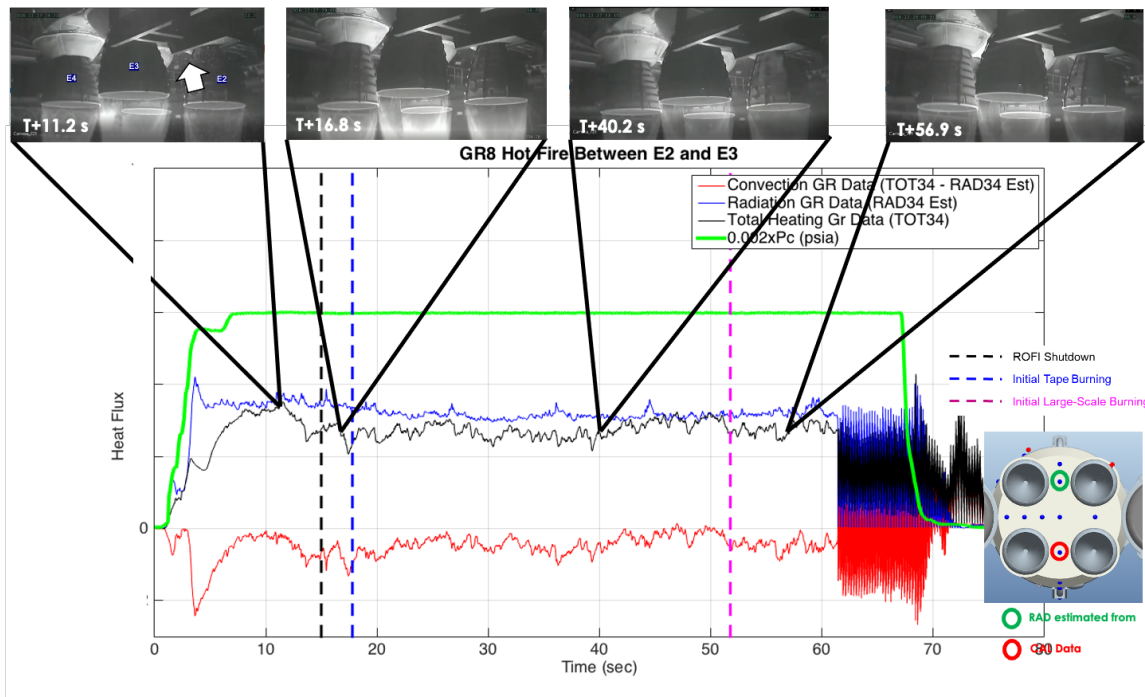


**Figure 11. (top)** base heat shield 034 total (black line) and radiative (blue line) heating data; overlaid with the RS-25 chamber pressure data (green line) and visual imagery data; White arrow shows approximate location of the DFI being assessed; base heat shield schematic shows location of the DFI being assessed

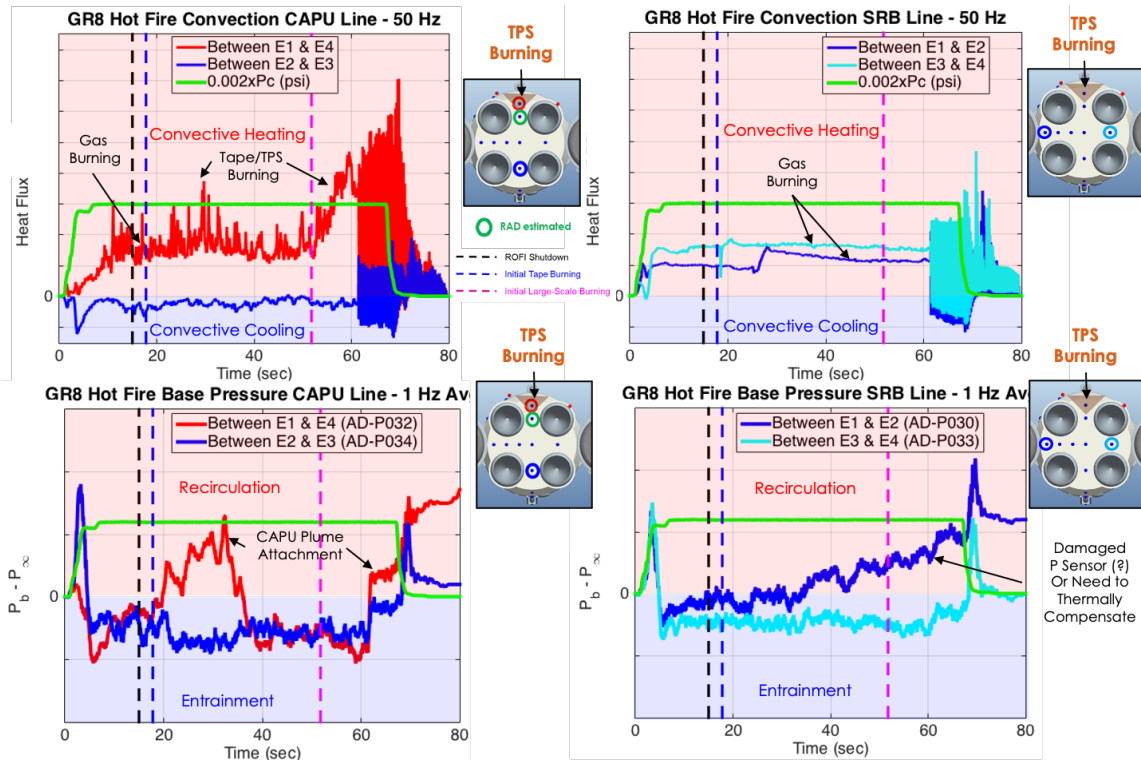


**Figure 12. (top-left)** GR HF1 convective heat flux vs. time between two DFI islands on the BHS near the CAPU ports; **(top-right)** GR HF1 convective heat flux vs. time between the two DFI islands near the SRBs; **1 (bottom-left)** GR HF1 differential base pressure vs. time between two DFI islands on the BHS near the CAPU ports; **(bottom-right)** GR HF1 differential base pressure vs. time between the two DFI islands near the SRBs; green line is the RS-25 chamber pressure

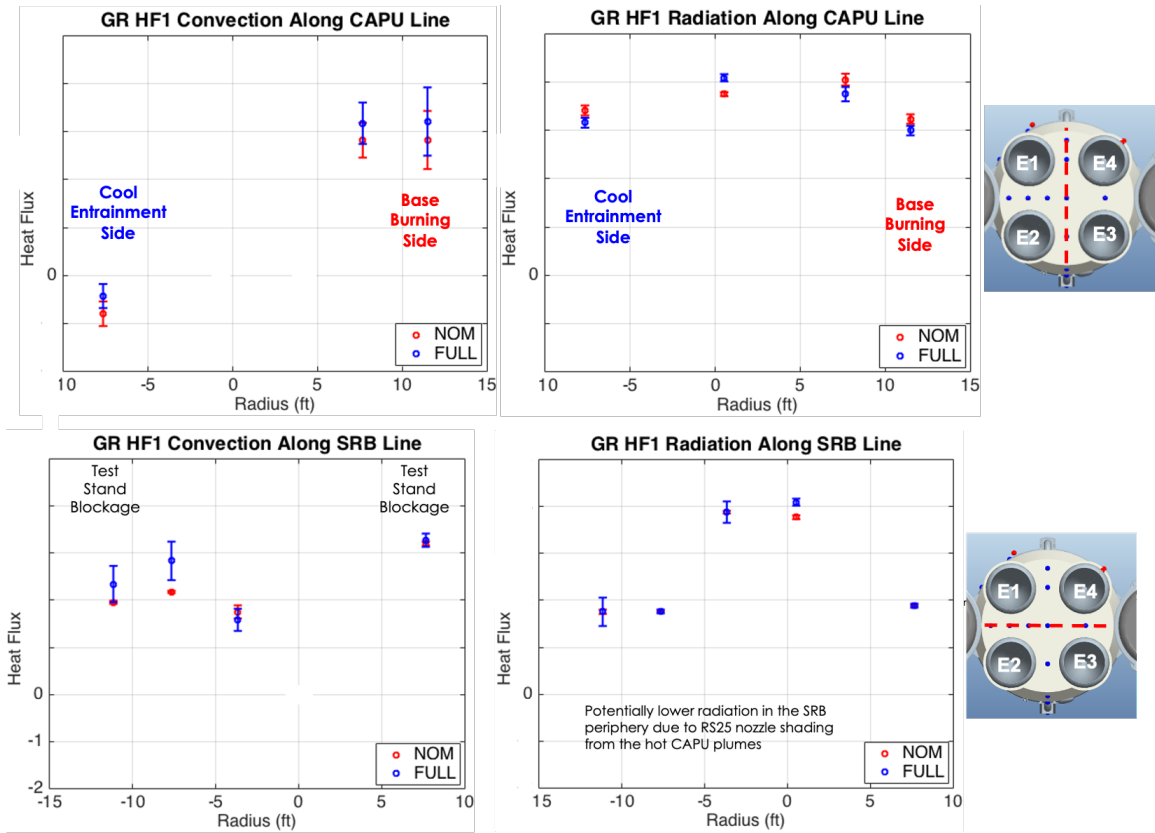


**Figure 13. (top)** GR HF1 convective and radiative heat flux vs. radial distance from the BHS centerline along the CAPU port axis; **(bottom)** GR HF1 convective and radiative heat flux vs. radial distance from the BHS centerline along the SRB axis

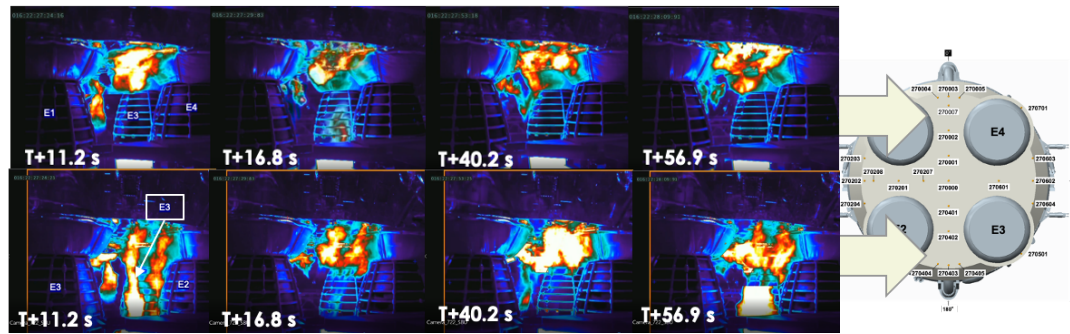


**Figure 14. (top)** IR imagery data showing CAPU flow field interactions with the base heat shield near E1 and E4; **(bottom)** IR imagery data showing CAPU flow field interactions with the base heat shield near E2 and E3

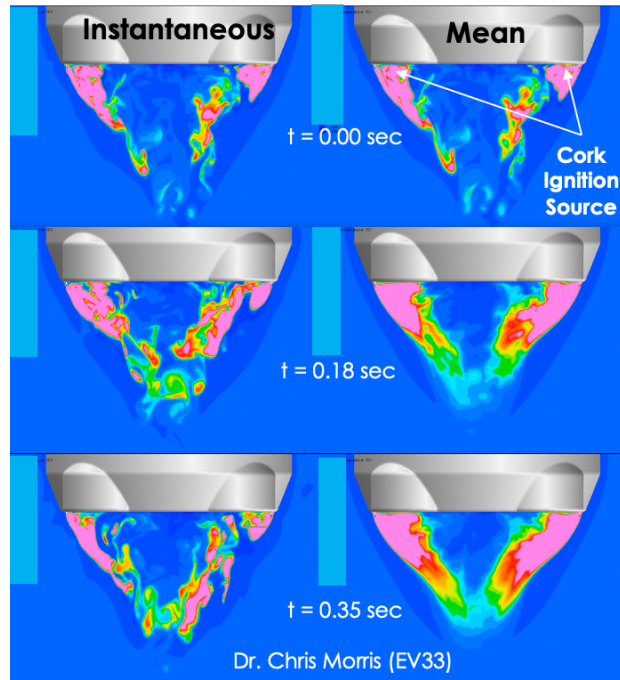


**Figure 15. Computational fluid dynamic simulation of the CAPU flow field during GR HF1 operation; Time-accurate 3D large eddy simulation (LES) [8-11]**

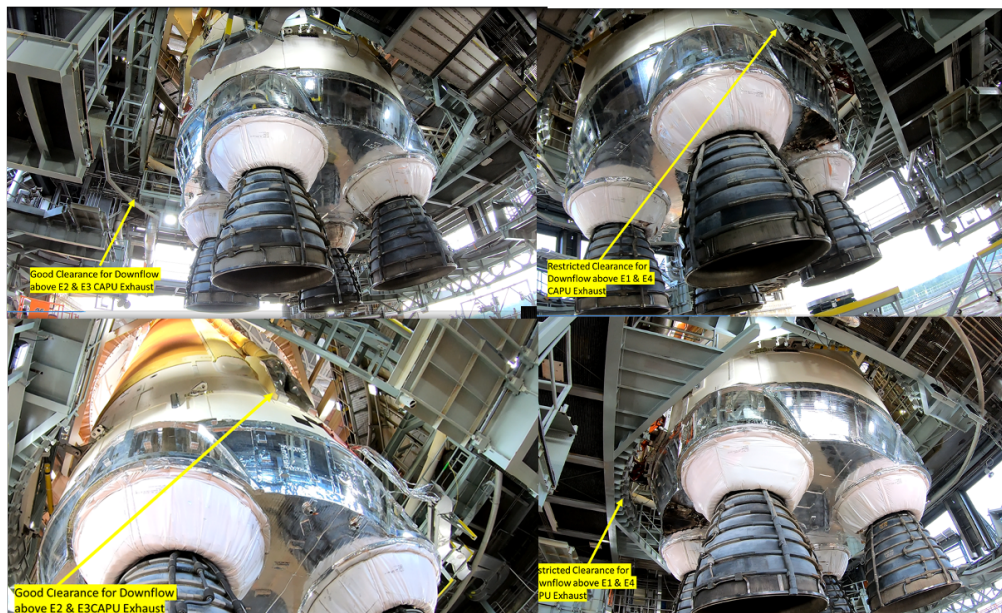


**Figure 16. NASA Stennis Space Center B-2 test stand fixtures relative to the Core Stage BHS for GR**

### **III. Green Run (GR) Hot-Fire 2 (HF2) Mitigation Approaches**

Since many of the hot-fire test objectives were not satisfied during GR HF1, the SLS Program decided on conducting a full-duration 500-sec hot-fire test for GR HF2. As a result, the Green Run BHS Anomaly Team was developed by the Core Stage leadership. The GR BHS Anomaly Team first developed technical rationale for the cause of tape and heat shield burning in GR HF1 as described above and then were actively challenged to develop mitigation plans to resolve this issue for GR HF2. There were two concerns: (1) how large could the convective heating be augmented due to TPS cork burning and (2) could TPS burning lead to a burn through of the heat shield during a full-duration test and compromise the integrity of the metal substructure? To minimize bringing mass to orbit, there is a thin membrane aluminum sheet substrate below the TPS heat shield. Hence, a burn through during flight could lead to deformation and failure of this membrane, resulting in vehicle failure.

There were two parallel analysis approaches taken to develop mitigation steps. The first one was to determine the amount and location on the heat shield where additional sacrificial cork would be needed to protect the metal substrate membrane. The second approach was to redesign the CAPU ports to minimize convective heating on the base heat shield. Redesign of the CAPU ports was investigated through the Dahm-Mayman analysis of flame behavior for coaxial fuel-air jets [14-15]. Dahm-Mayman analysis was supported by extensive measurements and test campaigns and the Feikema, Chen & Discroll paper [14] provided supporting measurements for H<sub>2</sub> – air flames. The C2 constant is a function of the maximum H<sub>2</sub> flame speed, thermal diffusivity, air-to-fuel ratio and density. This constant is needed to assess the blow-off velocity. The flame length is a function of the air-to-fuel velocity, density and diameter ratios. It also normalized with respect to the flame length of no coaxial velocity.

From the Dahm-Mayman analysis approach, the following parameters were calculated to inform CAPU port design [14-15]: (1) air blow-off velocity; (2) flame length; (3) flame lift-off height. Equations 2 through 7 show the analysis in predicting CAPU H<sub>2</sub> combustion flame dynamics for Green Run operation. Input conditions needed were the CAPU exit and air entrainment flow conditions which were obtained from GR HF1 and computational simulations. The air blow-off velocity was the air entrainment velocity that could lift and extinguish the H<sub>2</sub>-air flame. H<sub>2</sub> flame blow-off was deemed a risk because it would lead

to excessive buildup of unburned H<sub>2</sub> and a potential for detonating mixture. As a result, there was no design implemented to have the CAPU port and extension diverted outward from the base towards the entrained freestream. From the Dahm-Mayman analysis, the blow-off velocity was higher than the GR predicted entrainment flow conditions within the co-flow configuration as shown in Figure 17 [28-29]. The flame length also poses risk as noted in Figure 17. If the flame length is too short and close to the heat shield during air entrainment recirculation zone, the short flame can impinge onto the heat shield and significantly drive the convective heating. Based on input conditions for GR operation during CAPU low flow state, the Dahm-Mayman analysis shows that with the flight CAPU ports, the flame length is quite short and within the recirculation regime and can easily impinge on the heat shield, driving the convective heat load and TPS burning as observed for GR HF1. During the CAPU high-flow state, the flame lengths and blow-off velocities were quite large and did not pose a risk in terms of flame attachment to the heat shield and H<sub>2</sub> detonation. The goal was to make sure that the distance between the tip of the flame and the heat shield was outside the flow recirculation regime. This required that the CAPU ports have a long extension on the order of 2 feet. Based on analysis from the BHS Anomaly Team, it was recommended to have a straight CAPU extension directed downward away from the heat shield and recirculation zone. For GR HF2, as shown in Figure 18, aluminum CAPU extensions were fabricated for all four CAPU ports. Computational analysis was also conducted by Boeing to confirm these initial theoretical results. This analysis in conjunction with ease of fabrication of the extensions resulted in a path forward.

Second mitigation option was to assess the amount of sacrificial cork needed and the regions applied. Heat transfer or film coefficient within the large-scale fire regime was derived from the collocated DFI measurements such as the radiometer, calorimeter, gas temperature probe and the calorimeter reference temperature (Figure 19). From this, cold wall convective heating was derived from the 032 DFI island during the large-scale fire regime. Environments just prior to RS-25 engine shutdown were used. It should be noted that peak convection could not be assessed due to constant linear rise in convective heating and no observation of a heating plateau prior to engine shut-down. Once the radiative heat load disappeared upon engine shutdown, cork combustion ceased entirely. The GR HF1 large-scale fire environments were then applied in the E4/E1 region for a subset of the test duration based on when the tape and adhesive started burning. It was believed that cork burning would only occur once the Nexolve tape and adhesive burned,

but actual ignition dynamics was not characterized for this TPS. Based on updated large-scale fire heating environments provided to Boeing and thermal analysis assessment, it was recommended that a 1" sacrificial P50 cork was needed on top of the 1" baseline cork to protect the baseline heat shield and to prevent a burn through during a full-duration static-fire test.

As a result, the two mitigation paths, CAPU extensions and additional sacrificial P50 cork TPS, described above were the main mitigation approaches, but other methods were also employed to further reduce risk to the Stage during GR operation. The other approach adhered to was to heavily monitor the drag-on base substrate thermocouples and to make sure that the measurements were below 100 deg F during GR hot-fire operation. Other mitigation approach that was used were a slight redirection of the B-2 HBOI system to a more glancing impact to the heat shield than GR HF1 and the application of a more robust reflective tape, LT80 on the heat shield.

$$U_{a,BO} = U_f \left\{ \frac{\left[ \left( C_2 \frac{U_f}{d_f} \right)^{-2/3} - 1 \right]}{\left( \frac{d_a}{d_f} \right)^2 - 1} \right\}^{1/2} \quad (2)$$

$$L_f = d_f \left( \frac{L_f}{d_f} \right)_0 \left\{ 1 + \frac{\rho_a}{\rho_f} \left( \frac{U_a}{U_f} \right)^2 \left[ \left( \frac{d_a}{d_f} \right)^2 - 1 \right] \right\}^{-1/2} \quad (3)$$

$$C_{2,H2} = 4.8 \frac{\alpha}{S_{L,H2}^2} (1 + AF^{-2}) \left( \frac{\rho_f}{\rho_a} \right)^{-1/2} = 0.95 \mu sec \quad (4)$$

$$\left( \frac{L_f}{d_f} \right)_{0,H2} = f( Fr, AF, T_{ad,f}, T_\infty, U_f, \left( \frac{\rho_f}{\rho_a} \right) ) \quad (5)$$

$$h_{c,fire} = \frac{\dot{q}_T - \dot{q}_r}{T_g - T_w} \quad (6)$$

$$\dot{q}_{c,fire,CW} = h_{c,fire}(T_g - 459.7 \deg R) \quad (7)$$

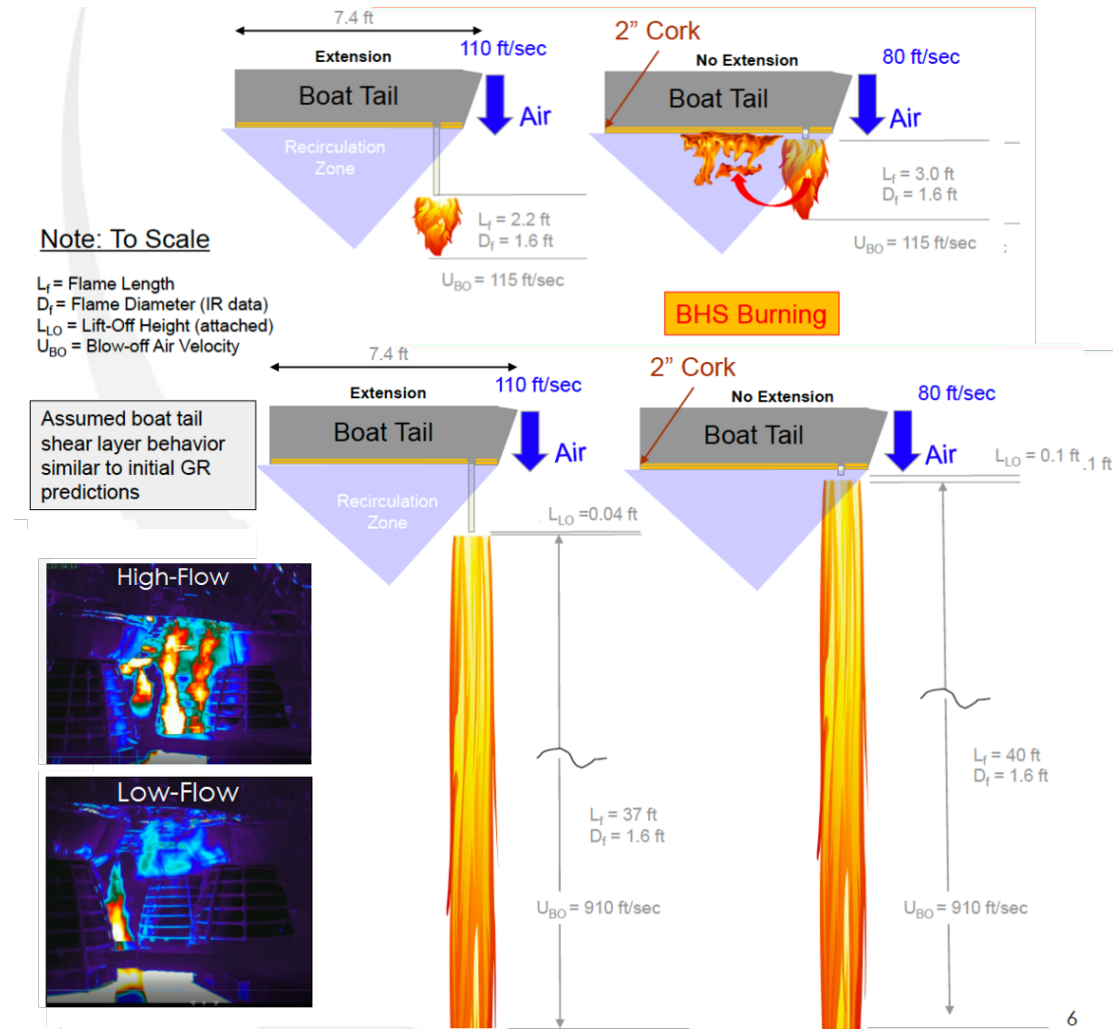
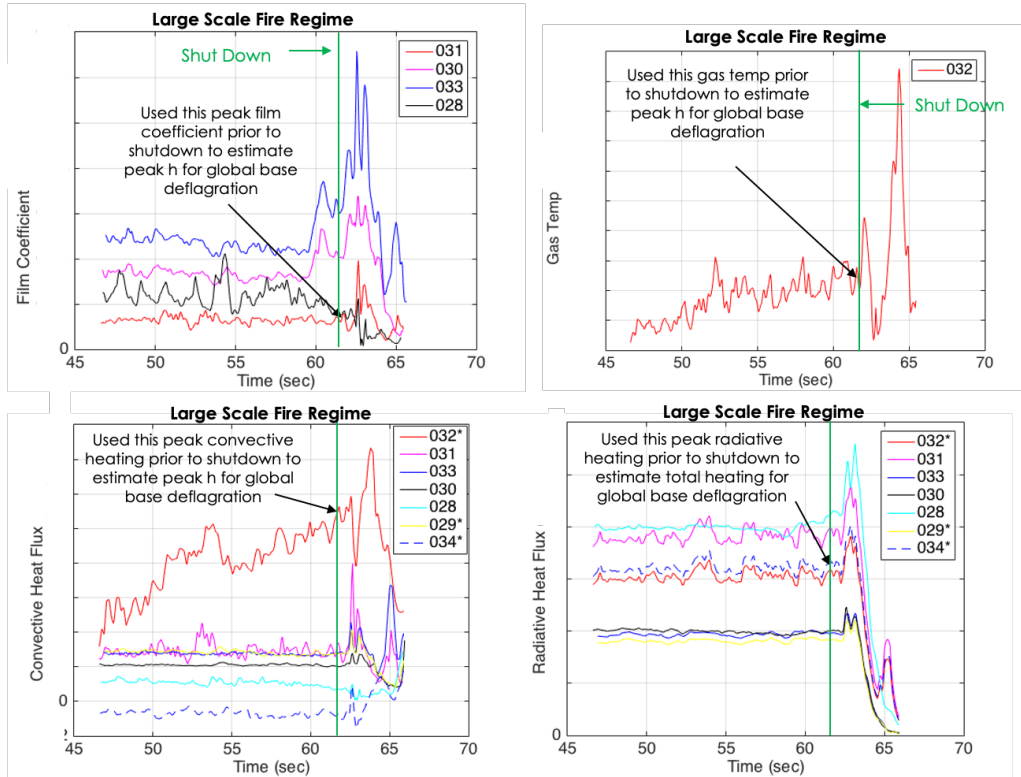


Figure 17. Theoretical analysis of co-flow flame dynamics for both the CAPU low and high flow states for both GR HF1 and longer CAPU extensions as a mitigating strategy



**Figure 18. (left) CAPU extensions to be applied for GR HF2; (right) CAPU extensions attached onto the Core Stage BHS for GR HF2**



**Figure 19. Large-scale BHS fire test-derived predicted environments: (top-left) film coefficient; (top-right) gas temperature; (bottom-left) convective heat flux; (bottom-right) radiative heat flux; environments based on GR HF1 large-scale fire data**

## **IV. Green Run (GR) Hot-Fire 2 (HF2) Base Heating Anomaly**

### **A. GR HF2 Core Stage Base TPS Configuration**

The Core Stage base was put in the GR HF2 TPS configuration to minimize refurbishment of the base secondary and primary structures. The LT80 reflective tape covered most of the base heat shield and boat-tail regions of the Stage to reduce incident radiation on the TPS and hardware. The E1/E4 region of the heat shield had 1' additional thickness of sacrificial cork TPS (a total of 2" of Hypalon/P50 cork) and it was not covered with LT80 tape as shown in Figure 20 (shown as brown). Inboard of this region, there was 0.7" of the exposed baseline TPS. Underneath the foil, there was 1.0" thickness of Hypalon/P50 cork wedges applied near the E2/E3 CAPU exhausts and 0.7" thickness of Hypalon/P50 cork applied everywhere else on the heat shield. Areas where there were gaps in cork or bolt bulkheads, RT455, a cork spray-on derivative, was applied in the shape of bricks. The thickness of RT455 applied for GR HF2 was a factor of ~2 greater than GR HF1 due to an increase in cork TPS thickness where there was no application of LT80 tape. This is shown as magenta rectangles in Figure 20. SOFI-180 foam was applied to seal the circular manhole cover, shown in yellow within Figure 20. This was the proposed base configuration for flight without the reflective foil and the SOFI-180 foam and the extra sacrificial cork which were applied specifically for the Green Run test campaign. Closeup of pre-test pictures of the GR HF2 base configuration can be shown in Figure 21. Note the careful application of the LT80 reflective tape to the base heat shield and boat tail regions of the Stage. No reflective tape was applied on the RS-25 engine blankets, shown in white within Figure 21. No rain shield barriers were applied to reduce the burning potential. All the DFI islands were covered with foil, but the sensor heads were exposed to capture test data. This figure shows the exposed Hypalon/P50 cork and RT455 regions, the CAPU extensions and the LT80 tape regions.

Although the mitigation approach of including CAPU extensions to reduce the convective heating was employed for GR HF2, large-scale deflagration of the entire base heat shield was first observed at the E1/E4 region at T+72 seconds. It was first perceived that the anomaly occurred due to a H<sub>2</sub> leak from the CAPU extension, but this was further reviewed after post-test and there was no structural damage with the CAPU ports. It was later hypothesized that the exposed P50 cork had reached its ignition heat load and

initiated the cork combustion. The highest heat load due to the burning was observed where sacrificial cork TPS was applied. The flame front then propagated toward the base center and then out to the periphery of the heat shield between E1 and E2 (Figure 22). The large-scale flames engulfed out to the periphery of the heat shield between E2 and E3. The flames never reached the heat shield between E3 and E1. Once the test was completed and the engines shut-down at 500 seconds, the flames immediately ceased. However, extensive charring of the heat shield was observed that mapped out the footprint of the burning as shown in Figure 22. The charring had an alligator skin quality and all the RT455 had ablated away to the thickness of the cork. However, in the region between E1/E4, some residue of the Hypalon can be seen. Although extensive charring was observed, the TPS performed its function as an insulator and protected the thin underlying metallic structure from exceeding its' temperature requirement. Due to a static test condition and very low shear stress (less than 0.1 psf) and Mach Number, post-test measurement showed limited to no ablation of the char layer during the GR HF2.

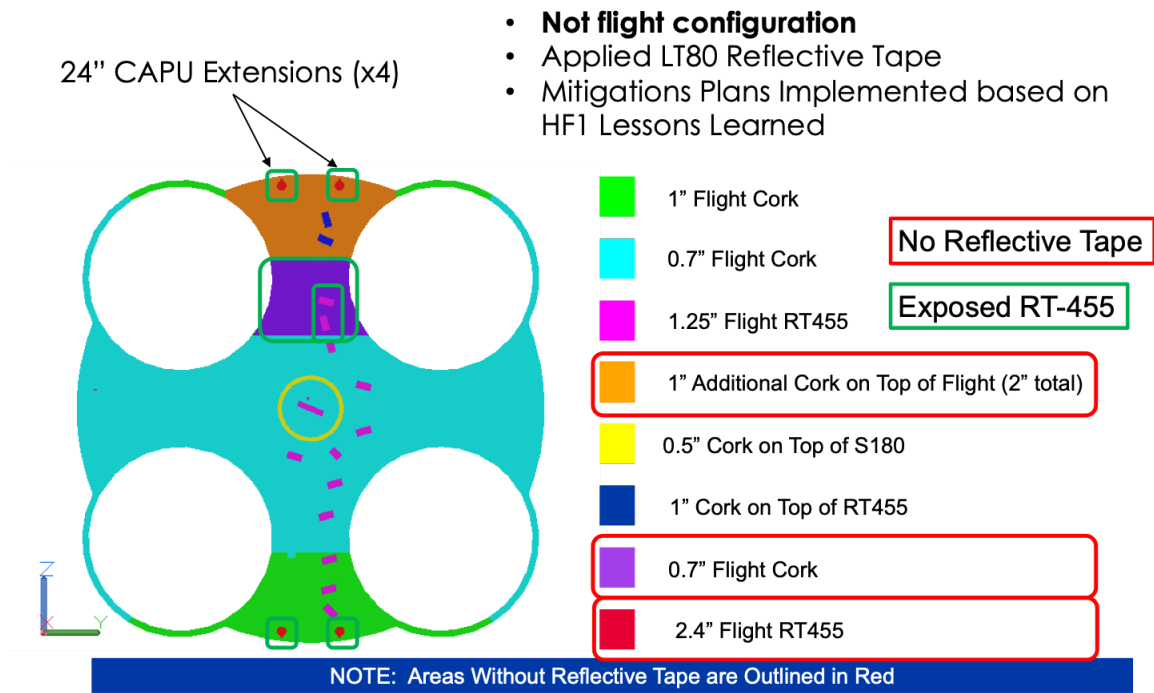


**Figure 20. Green Run Hot Fire 2 base TPS configuration**

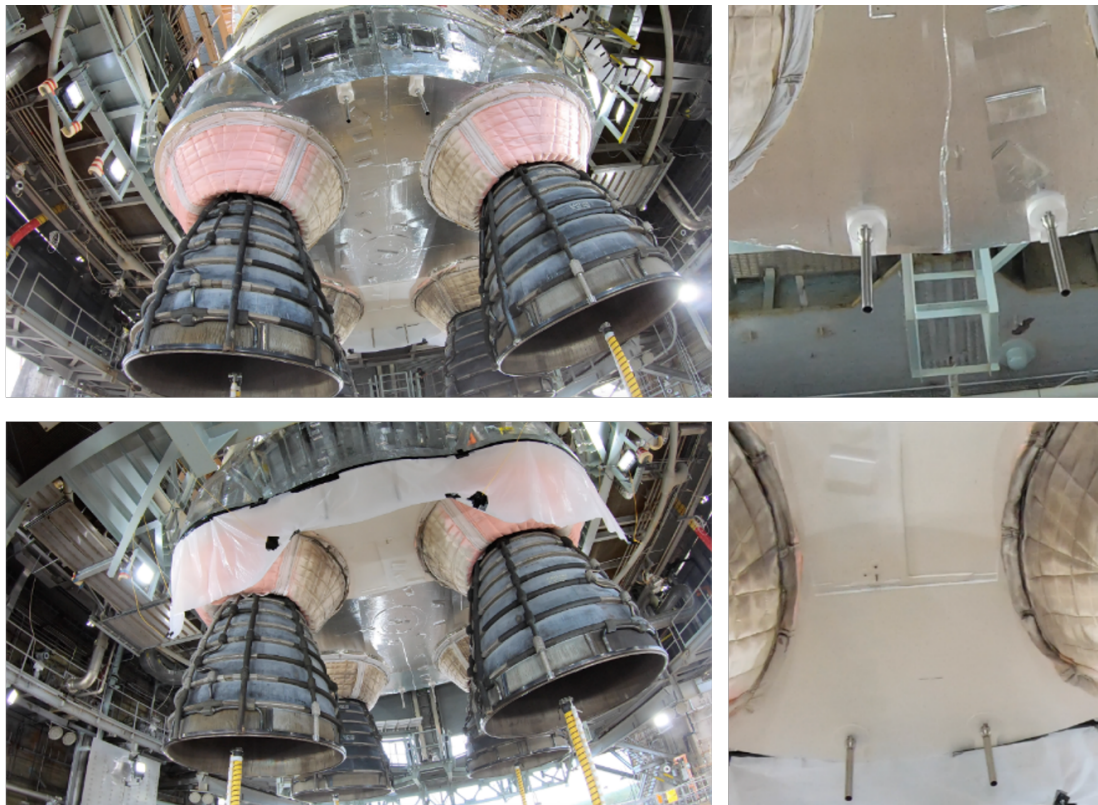


**Figure 21. Pictures of the Core Stage BHS configuration for GR HF2**



**Figure 22. (left) GR HF2 post-test observations of the Core Stage BHS; (right) three time-evolution VIS images of TPS cork combustion of the entire BHS during GR HF2 test operation**

### B. GR HF2 Core Stage Base Aerothermodynamics Reconstruction

Reconstruction of GR HF2 base heat shield environments was pursued to fully understand the anomaly and the TPS ignition dynamics. A few methods described above were employed to reconstruct the aerothermal environments. The additional goal of conducting an accurate reconstruction effort was to then update the base heating models from GR lessons learned if needed. There were two objectives to the reconstruction effort that would impact Artemis I: (1) assess TPS ignition dynamics and determine if flight ascent environments would lead to base heat shield cork combustion/deflagration and (2) if such flight conditions did support these phenomena, provide updated convective and radiative base environments for ascent. Redesign of the base heat shield would require additional work, time and analysis and so the BHS

Anomaly Team had to quickly assess the base flow physics and associated environments in-time to support the launch.

Reconstruction of the island 027, the base heat shield center, shows significant augmentation in convective heating after T+210 seconds due to Hypalon/P50 cork combustion (Figure 23). This discontinuous increase in total and convective heating is due to the sudden ignition of the Hypalon/P50 cork. The average convective heating is 4x the nominal heating values prior to TPS ignition. An active flame front within the base center is supported by visual imagery data as well. There is an overshoot in the total/convective heating due to burning of the Hypalon paint. However, the high convective heating does not dissipate with time and plateaus at ~T+300 seconds. This region showed the highest total and convective heating on the base heat shield. One theory is the extensive amount of air that is entrained from the four vent paths, leading to a higher local O/F ratio closer to stoichiometric values. The combustion occurs near stoichiometric point, but the increased mass flux of entrained air leads to an increase in reactant concentration and larger combustion heat release. This would enable higher gas temperatures and convective heating rates. Although the flame front diminishes with time, the TPS is still smoldering with flamelets leading to sustained and relatively constant high convective heating. The GR HF2 base heating data during cork combustion was invaluable in providing the amount of heat release due to char oxidation and pyrolytic gas burning. Although this provided a steady-state heat release term, it was specific to the GR static test conditions (local O/F ratio) at sea-level. Prior to cork ignition, the convective and radiative heating were relatively constant as shown in Figure 23. It should be noted that the convective heating after cork ignition is reporting total heating since the radiometers have failed at this point. The convective heating is estimated based on collocated calorimeter and radiometer shown on Equation 1 on page 16.

GR HF2 analysis of island 031, region between E1 and E4, shows similar observations to island 027, but cork ignition occurs much earlier in test at T+72 seconds (Figure 24). Also, there is a large increase in total and convective heating upon ignition and then reaches a lower heating steady-state value. This could be due to two effects: (1) active flame front on the base heat shield and then the smoldering phase which shows a more diminished heating effect; (2) Hypalon burns more vigorously, leading to higher combustion temperatures than the P50 cork combustion event. One other thing to note at 50 Hz sampling rate, total heat flux data is quite noisy during the cork combustion phase due to the unsteady flame dynamics on the heat

shield. Note that noisy data was not observed during nominal environments. IR imagery data clearly shows the flame front on the heat shield and the high TPS surface temperature during cork combustion.

One area that needs further investigation is that the base radiometers all failed when the cork combustion process ensued. None of the radiometers provided any response and it is hypothesized that the cork combustion products and soot deposited over the sapphire window disabling the ability to measure incident radiation from the four RS-25 Mach discs. No direct measurement of the radiation component during the TPS cork combustion process could be extracted from GR HF2. However, nominal radiation prior to cork ignition was measured.

Hypalon/P50 cork combustion was also observed at island 030, periphery of the heat shield between E1 and E2, at T+320 seconds supported by significant increase in total/convective heat flux and imagery data (Figure 25). All 6 base heat shield DFI islands support cork combustion environments except island 032 and 033 due to the fact that they were either not operational or the flame front had not reached to their region prior to engine shutdown. Further evidence of the cork combustion ignition and environments can be supported by the base gas temperature data. It can be seen from Figure 26 that there is a spike in the base gas temperature from a nominal ambient to many factors above ambient upon TPS cork ignition. The high boundary layer gas and potential flame temperature is sustained during the entire cork combustion process. This is an interesting observation; the smoldering phase has a diminished flame front, but the boundary layer gas temperature is still elevated. The gas temperature distribution is similar to the total/convective heating distribution where there is an overshoot during ignition and then a lower baseline is established. As expected upon the cork ignition, the calorimeter body thermocouple shows a discontinuity in the wall temperature and shows linear increase during the combustion regime (Figure 26).

Although not quantified in this paper, the two parameters to define cork ignition is the total heat load and threshold heat rate which supports the ignition dynamics. This is under the assumption that the initial TPS surface temperature is near ambient for all comparisons. The main driver in predicting cork combustion environment is the TPS surface temperature, but that data is not always readily available. As the heat load increases and results in increases in the TPS surface temperature, both pyrolytic gases that escape the TPS and char react with oxygen from the air to lead to a large energy release and large-scale deflagration. This sudden increase in convective/total heating provides energy feedback to the TPS to

continue the combustion process. Further ground test campaigns have been planned to fully investigate Hypalon/P50 cork ignition and flame-out dynamics as a function of incident heating rates, ambient pressure, and air entrained flow rates.

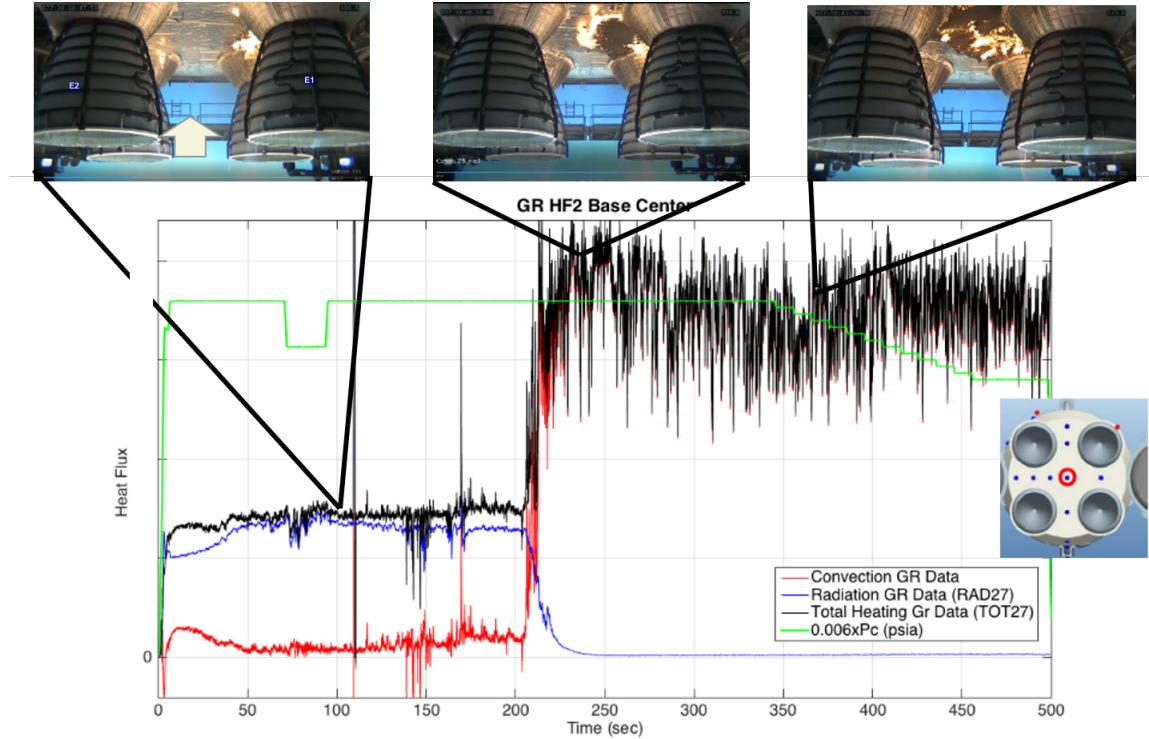


**Figure 23. (top) visual imagery data; (bottom) GR HF2 base heat shield 027 total (black line) and radiative (blue line) heating data; overlaid with the RS-25 chamber pressure data (green line) during GR HF2; all convective heating plots are estimated based on collocated sensors and convective heating plot is recording total heating during the cork combustion regime; this applies to all GR HF2 BHS environments shown below; White arrow shows approximate location of the DFI being assessed; base heat shield schematic shows location of the DFI being assessed**

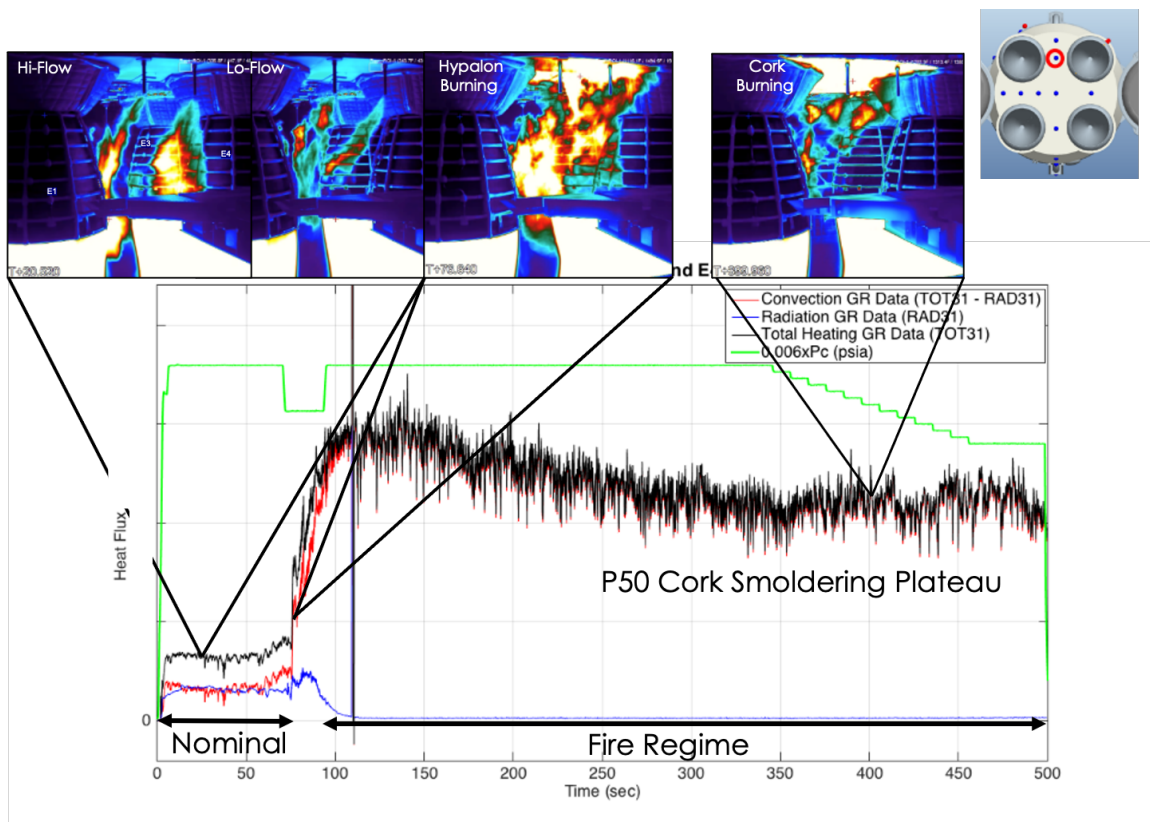


**Figure 24.** (top) IR imagery data; (bottom) GR HF2 base heat shield 031 total (black line) and radiative (blue line) heating data; overlaid with the RS-25 chamber pressure data (green line) during GR HF2; all convective heating plots are estimated based on collocated sensors and convective heating plot is recording total heating during the cork combustion regime; base heat shield schematic shows location of the DFI being assessed

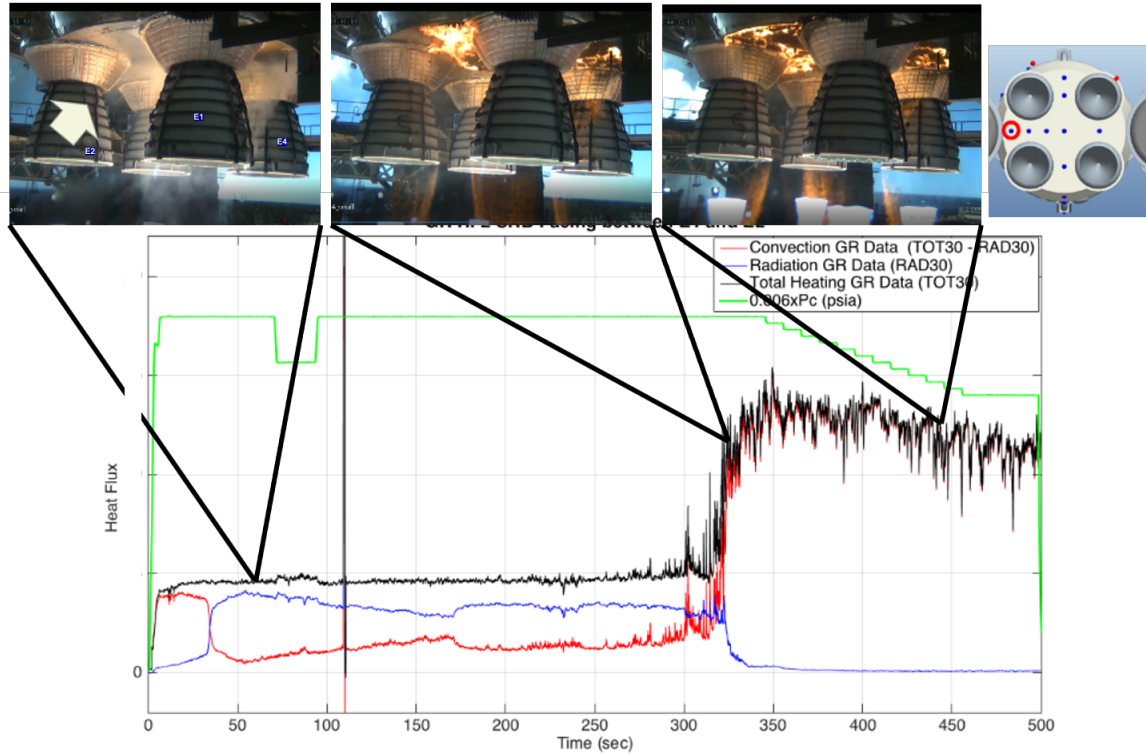


**Figure 25.** (top) visual imagery data; (bottom) GR HF2 base heat shield 030 total (black line) and radiative (blue line) heating data; overlaid with the RS-25 chamber pressure data (green line) during GR HF2; all convective heating plots are estimated based on collocated sensors and convective heating plot is recording total heating during the cork combustion regime; white arrow shows approximate location of the DFI being assessed; base heat shield schematic shows location of the DFI being assessed

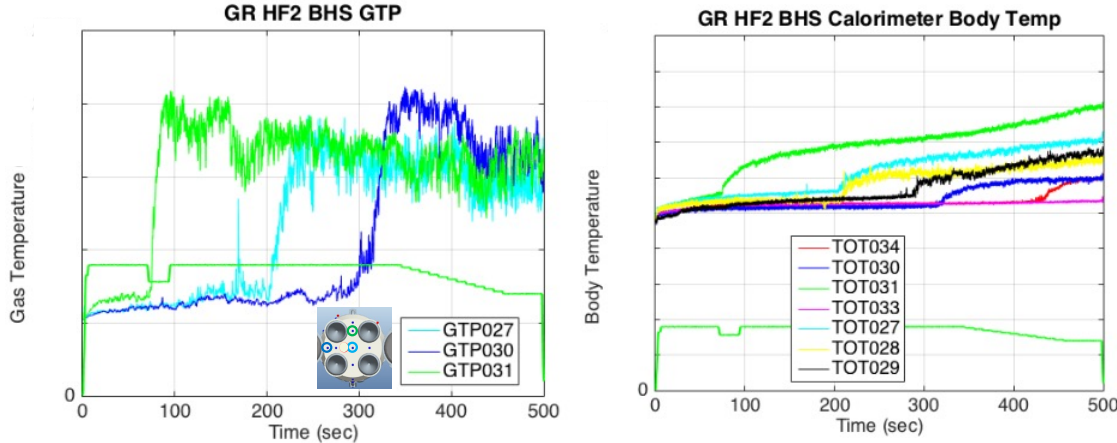


**Figure 26. (left) GR HF2 base gas temperature vs. time; (right) GR HF2 BHS calorimeter body temperature vs. time**

### C. GR HF2 Base Aerothermodynamics and TPS Analysis and Observations

Figure 27 shows a comparison of convective heat flux and surface pressure differential as a function of time in the same region of the heat shield during GR HF2 operation. The raw 50 Hz surface pressure data was successfully passed through a moving-average filter to reduce the noise in the data. Convective base cooling occurs due to base flow entrainment for a few pressure transducers such as P027, P030 and P033. The four RS25 engines aspirate the base flow air. Aspiration occurs when the base pressure differential ( $P_b - P_{inf}$ ) is negative and local base recirculation occurs when there is a positive base pressure differential. CAPU H<sub>2</sub> flame impingement can also lead to a positive base pressure differential and convective heating (Figure 27). It can be seen that during large-scale fire regime there is a large increase in the differential base pressure and convective heat flux. As the boundary layer gas temperature increases, the surface pressure increases due to the energy release during char and pyrolysis gas oxidation. In some instances, there is a base pressure lag with respect to peak convective heating. Cork combustion has large effects on convective heating, base pressure and gas temperature parameters and as a result a new environment is developed from these strongly TPS-base flow coupled physics.

To further understand if cork combustion environments pose a separate environment than plume-only induced dominant mechanisms such as radiation, aspiration and recirculation, Figure 28 shows

the differences between plume-centric dominant mechanisms and plume-TPS coupled base flow mechanisms. From GR HF2, it can clearly be seen that the plume-TPS coupled base flow physics results in much higher convective heating than the predominant plume-centric mechanisms for all DFI islands where data was collected. This significant augmentation in convective heating was observed along the SRB and CAPU lines as shown in Figure 28. The cork TPS combustion environments are an order of magnitude higher than the convective heating observed prior to cork ignition. This results in higher complexity in predicting plume-induced base flow environments as now a two-way coupling of energy and momentum need to be considered between the plume and TPS. GR HF2 did not provide insight into the behavior of radiation due to cork combustion processes.

To assess if the mitigation strategies provided some benefit to the environments, Figure 29 shows that the CAPU extensions reduced the convective and total heat rates within the E4/E1 region, island 031, where the cork burning was first initiated during GR HF1. This was a predicted outcome based on both theoretical and computational analysis. Base gas temperature and radiation were also considerably lower for HF2 than HF1. Convection was also reduced for island 030, near the periphery of the heat shield between E1 and E2 (Figure 30). However, total heating was similar between HF1 and HF2. CAPU extensions mitigated high heating in this region, but it had a smaller impact in other regions of the heat shield. IR imagery shows that CAPU extensions prevent H<sub>2</sub> flame attachment and impingement on the heat shield during CAPU operations in the low-flow state, reducing the probability of early onset TPS burning (Figure 31). Unsteady large-eddy simulations (LES) also show that the CAPU extension prevent H<sub>2</sub> flame attachment and impingement on the heat shield in the CAPU low flow state as shown in Figure 32 [8-11]. There is no H<sub>2</sub> flow recirculation observed between the CAPU exit and the base heat shield. As a result, HF2 cork burning was delayed by 20 seconds as compared to HF1. The goal was to minimize the convective heating. Although the CAPU extensions performed as designed, the radiative heating was not mitigated within the E1/E4 region which was the driver in cork combustion. Once the cork combustion initiated within the E1/E4 region where bare cork was exposed, the high energy flames melted and ripped the LT80 tape, further exposing the TPS to the radiative and convective environments. This led to the cork TPS flames progressively moving inward and then engulfing throughout the base heat shield.

The investigation of base heat shield TPS response was also conducted. The extensive spatial charring was observed through visible imagery data, but char depth was not initially known. Boeing at the request of NASA measured the char and pyrolysis layer thickness by sanding the compromised layer next to a few of the aerothermal sensors. Figure 33 shows both the recession rate and the total pyrolysis/char layer vs. total heating rate for GR HF2. Recession rate is estimated assuming that both the char and pyrolysis layers are ablated for conservatism. Less than 0.25" depth of the 1" and 0.7" P50 cork had been charred due to base heating environments over 500 seconds. The reason the char/pyrolysis layer thickness was smaller than prediction was due to the very low base shear stress and Mach number during GR HF2 and static test conditions (shown in Figure 33). Equations 8 – 15 develops the methodology through compressible Bernoulli and Reynolds Analogy equations in estimating the base flow Mach number and wall shear stress from DFI data [13]. Pressure and gas temperature data in the periphery, freestream and base center were used to make these estimates. The shear loads on the char are not strong enough to liberate the char that can lead to large ablation rates. For instance, there is very little evidence of shear effects on char due to the predominant alligator skin topology (Figure 22). This is characteristic of low shear – high heating environments. With the char layer mostly intact during Green Run this leads to an ideal insulative layer minimizing the heat to propagate into the TPS. For instance, if there was ablation and charring actively occurring due to higher shear stress loads, the char layer would have penetrated deeper into the TPS. The shear loads and ablation rates in flight will be substantially higher than GR HF2 due to much higher entrainment from both effective ejectors of the RS-25 and RSRMV motor plumes and the vehicle reaching supersonic velocities and the supersonic base flow during peak recirculation and choked flow regimes.

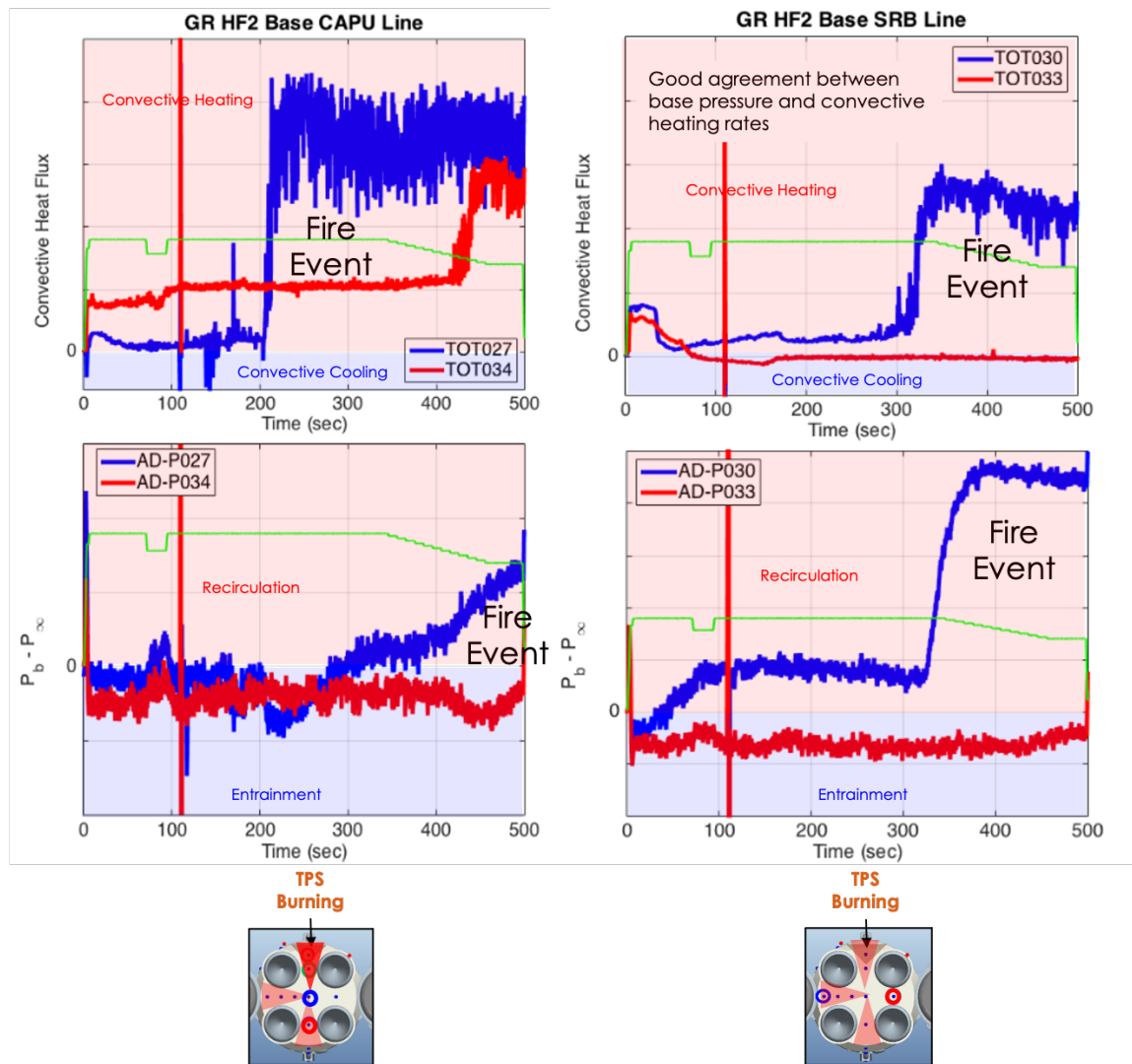


**Figure 27. (top-left)** GR HF2 convective heat flux vs. time between two DFI islands on the BHS near the CAPU ports; **(top-right)** GR HF2 convective heat flux vs. time between the two DFI islands near the SRBs; **1 (bottom-left)** GR HF2 differential base pressure vs. time between two DFI islands on the BHS near the CAPU ports; **(bottom-right)** GR HF2 differential base pressure vs. time between the two DFI islands near the SRBs; green line is the RS-25 chamber pressure

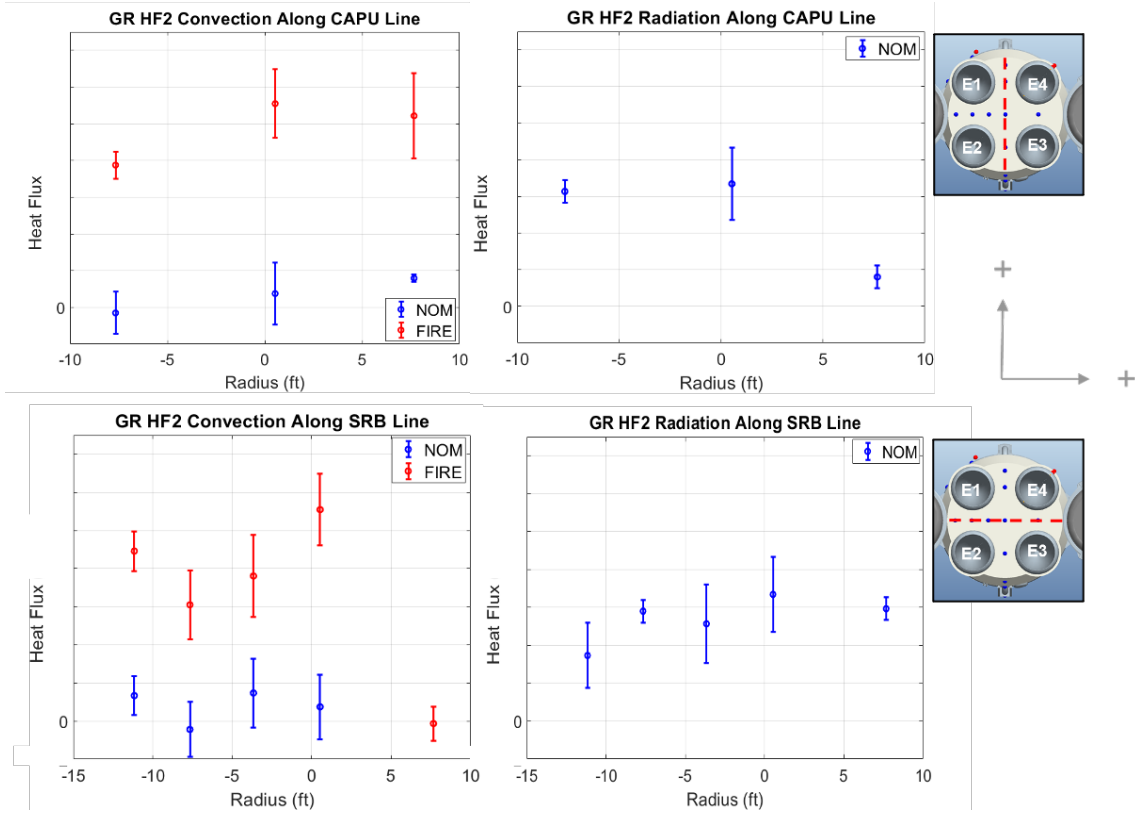


**Figure 28. (top) GR HF2 convective and radiative heat flux vs. radial distance from the BHS centerline along the CAPU port axis; (bottom) GR HF2 convective and radiative heat flux vs. radial distance from the BHS centerline along the SRB axis; NOM = nominal environments and FIRE = large-scale fire environments**

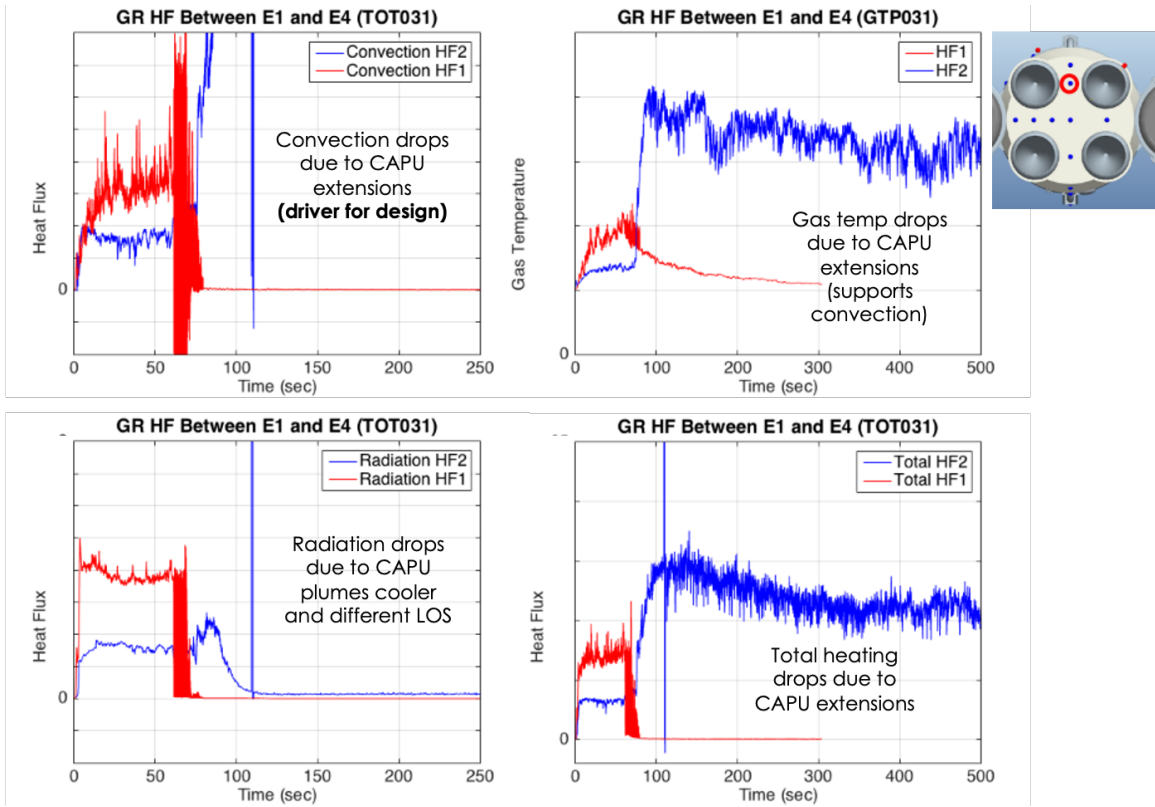


**Figure 29. Core Stage BHS environments between HF1 and HF2:** (top-left) convective heat flux; (top-right) base gas temperature; (bottom-left) radiative heat flux; (bottom-right) total heat flux; all plots shown as a function of time during test operation for the 031 island DFI between E1 and E4.

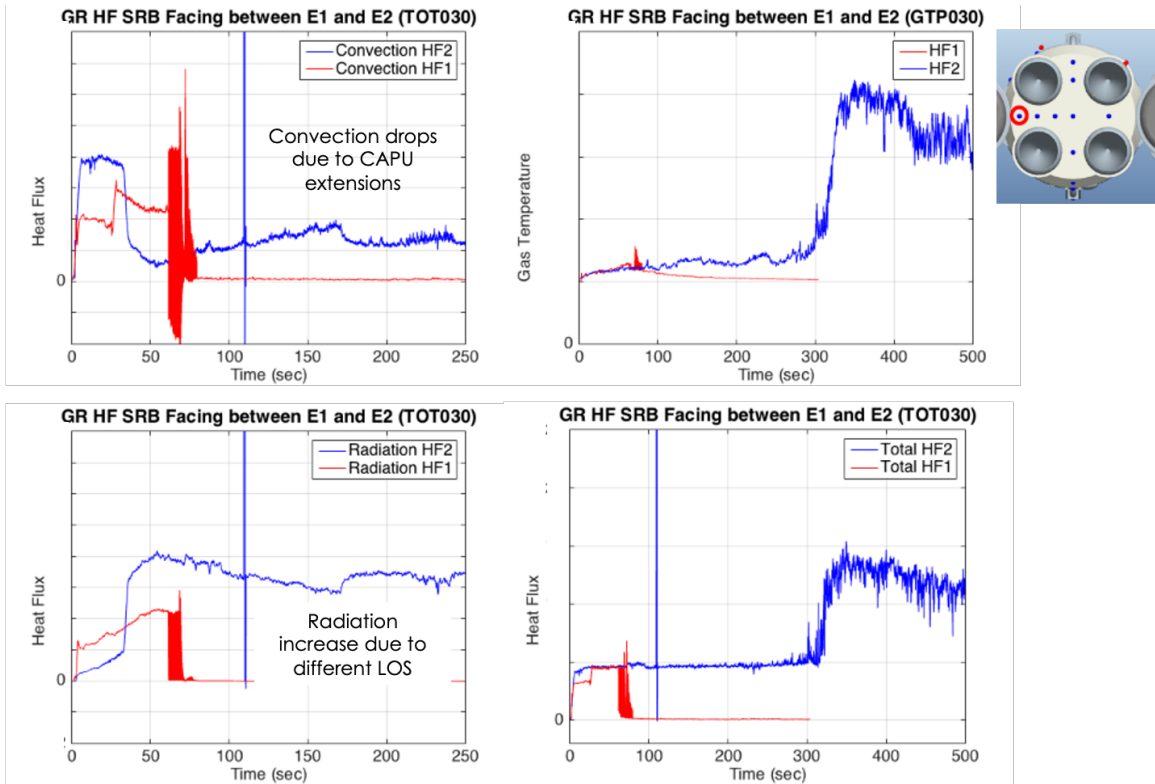
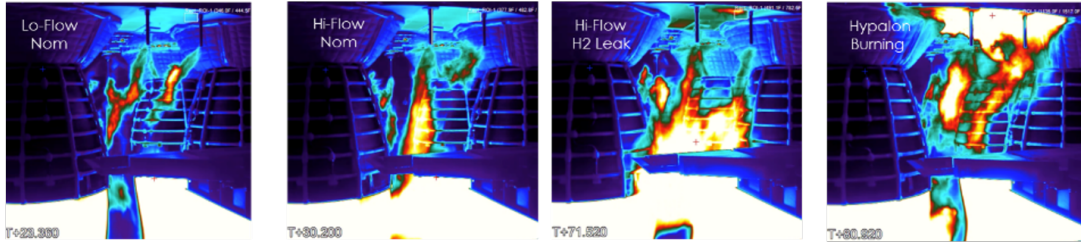


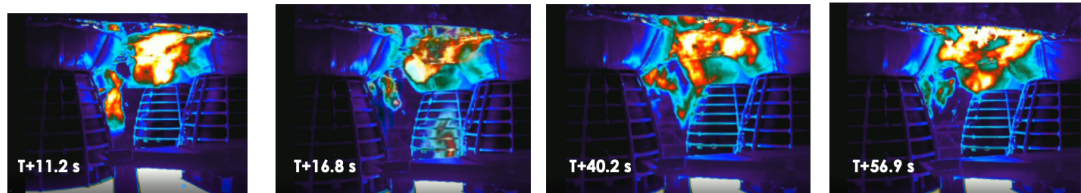
**Figure 30. Core Stage BHS environments between HF1 and HF2:** (top-left) convective heat flux; (top-right) base gas temperature; (bottom-left) radiative heat flux; (bottom-right) total heat flux; all plots shown as a function of time during test operation for the 030 island DFI near the left SRB.

- Based on IR imagery data and DFI convective heating environments, CAPU extensions performed as designed

HF2 (CAPU Extension Design & Other Mitigation Plans)



HF1 (Nexolve Tape in Flight Configuration)



All IR/VIS imagery provided by Darrell Gaddy (ER43)

**Figure 31.** CAPU extension mitigation strategy: (top) IR time-evolution images of the CAPU plumes with extensions during GR HF2; (bottom) IR time-evolution images of the CAPU plumes without extensions during GR HF1

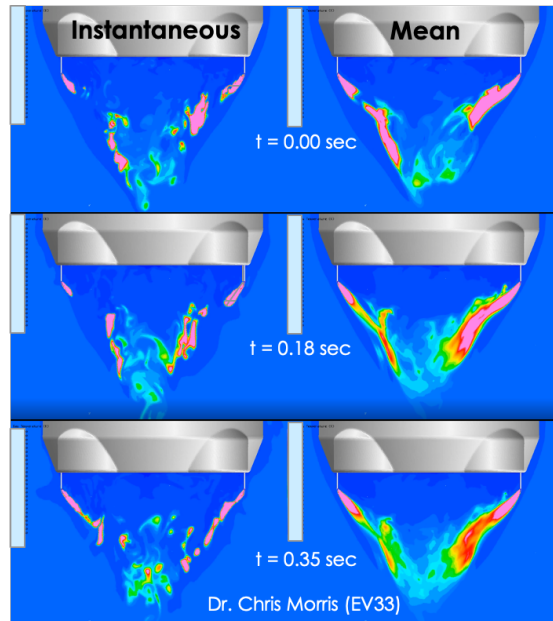


**Figure 32.** Computational fluid dynamic simulation of the CAPU flow field during GR HF2 operation; Time-accurate 3D large eddy simulation (LES) [8-11]

$$\frac{P_{center}}{P_{periphery}} = \frac{P_0}{P_J} > 1 \text{ & } H > 50,000 \text{ ft} \quad (8)$$

Assume 100% water vapor

$$Ma_J = \sqrt{\frac{2}{\gamma_J(T_{rec})} \ln\left(\frac{P_0}{P_J}\right)} \quad (9)$$

$$\frac{P_0}{P_J} < 1 \text{ & } H > 61,000 \text{ ft} \quad (10)$$

Assume 100% water vapor

$$Ma_J = -\sqrt{\frac{2}{\gamma_J(T_{rec})} \ln\left(\frac{P_J}{P_0}\right)} \quad (11)$$

$$\frac{P_0}{P_J} < 1 \text{ & } H < 61,000 \text{ ft} \quad (12)$$

Assume 100% air

$$Ma_J = -\sqrt{\frac{2}{\gamma_J(T_{rec})} \ln\left(\frac{P_\infty}{P_0}\right)} \quad (13)$$

$$\frac{C_f}{2} = \frac{Nu}{RePr^{1/3}} \quad (14)$$

$$\tau_w(H) = \frac{hU_j\mu}{kPr^{1/3}} \quad (15)$$

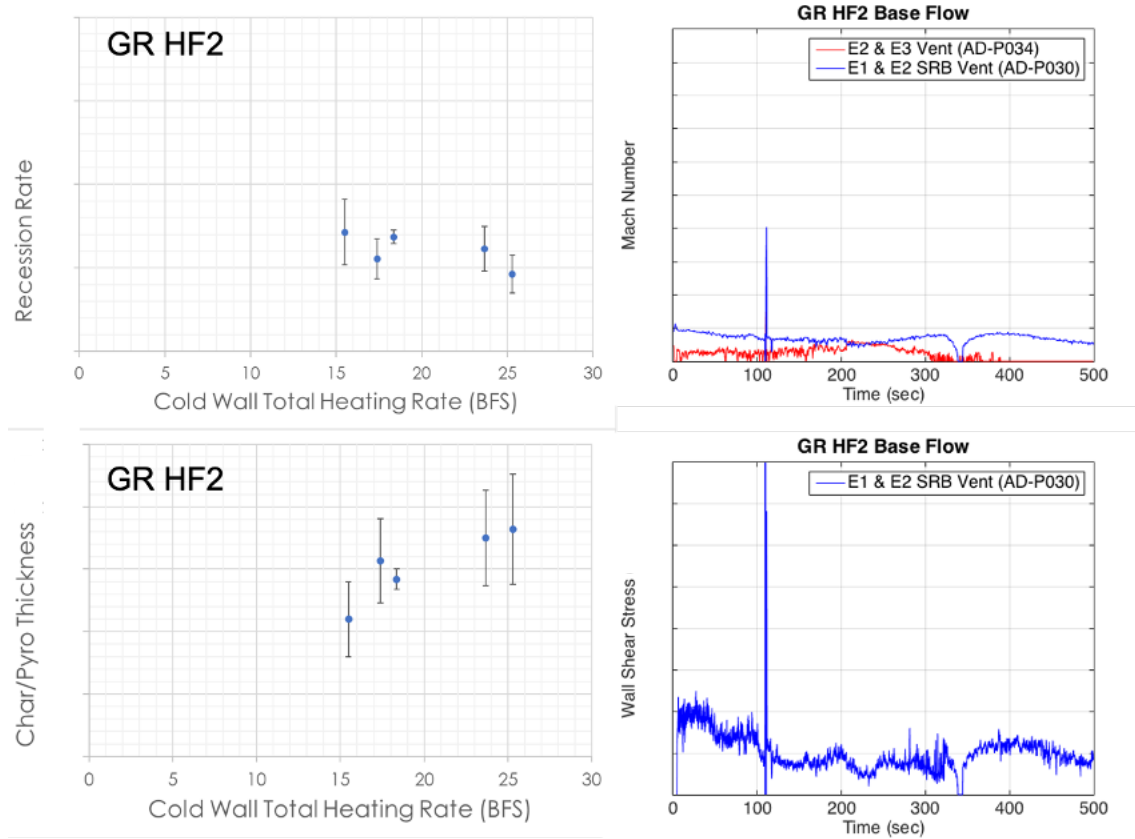


**Figure 33. GR HF2 base heat shield TPS response and shear stress:** (top left) base heat shield TPS recession rate vs. cold wall total heating rate; (bottom left) total char/pyrolysis layer thickness vs. cold wall total heating rate; (top right) estimated base flow Mach number; (bottom right) estimated wall shear stress

## V. Post-Green Run (PGR) Base Heating Models and Artemis I (AR01) BHS Redesign

### A. Plausible Evidence of BHS Cork TPS Combustion during AR01 Ascent

Prior to the GR test series, TPS cork combustion was not accounted for as a separate heating source in the SLS BHS thermal design environments for ascent. The traditional approach of plume-only heating environments combined with conservative test-derived cork recession models was deemed sufficiently conservative. However, large convective heating magnitudes and widespread extent of cork TPS deflagration observed during GR HF1 and HF2 persuaded the Team to consider cork combustion as a

realistic scenario for flight. As there was no observation of cork combustion environments specific to the SLS vehicle during ascent, plausible evidence of this environment was needed prior to updating the current base heating models and base heat shield redesign. A few theories were made to counter this phenomena in flight: (1) cork combustion environment is specific to the static hot-fire test configuration and would not ensue during ascent; (2) the base flow Mach number and shear stress would be high enough during ascent to extinguish the flame front; (3) those observations are due to either H<sub>2</sub> burning with the freestream and base gas recirculation. However, two technical points were supportive of the possibility of this phenomena occurring in flight.

First, there were some earlier ground test campaigns that showed cork combustion with some cross flow occurring at sea-level due to a strictly radiative source. The MSFC thermal vacuum chamber test campaign in 2017 first observed P50 cork combustion due to a radiative heat load and minor convective cooling at sea-level conditions. An attached flame front on the TPS cork was observed after certain duration in testing. Unfortunately, there was no measurements of the convective and radiative environments obtained and limited sensitivity studies conducted. This lab-based test campaign led to applying reflective tape on the SLS base to minimize the radiative heat load, cork combustion and refurbishment during Green Run. At the time, there was no data showing the combustion process due to changes in ambient pressure, incident radiative heat rate and air entrainment velocity. Also, Delta IV heavy shows base cork combustion during lift-off and ascent, but NASA did not have details of the ignition and flameout dynamics and aerothermal environments.

Second, it should be noted that the SLS vehicle during ascent has many sources of fuel, oxidizer and ignition for base heat shield TPS burning (Figure 34). For instance, CAPU H<sub>2</sub> burning with air and forming hot CAPU plumes leads to a non-negligible convective heating component especially when the flames are attached to the heat shield. Incident radiation from the RS-25, SRB and CAPU plumes magnifies the radiative heat load on the Core Stage base. It should be stressed that LT80 reflective (low emissivity) tape will not be applied on the base heat shield for the flight configuration and the Hypalon/P50 cork will be directly exposed to all the elements and environments. The SRB plumes generate the highest radiation source due to a high concentration of hot aluminum-oxide particulates. The predicted SRB radiation is 3X the radiation of the RS-25 plumes at lift-off. As a result, the radiative heating and heat load during ascent

will be many factors higher than observed during GR HF1 and HF2. Initial ignition of the P50 cork further increases the convective and total heat load on the TPS due to high oxygen availability in the freestream, leading to a positive feedback loop in increasing the TPS surface temperature and sustaining the combustion environment. The flight environment poses harsher aerothermal environments than during GR from both convective and radiative components. After extensive research into some historical ground test and flight imagery data and knowledge of the SLS ascent configuration and predicted environments, cork TPS combustion base heating models needed to be accounted for during AR01 flight. The updated base heating models would be derived from GR HF1 and HF2 flight-scale test data in conjunction with the baseline wind-tunnel derived models.

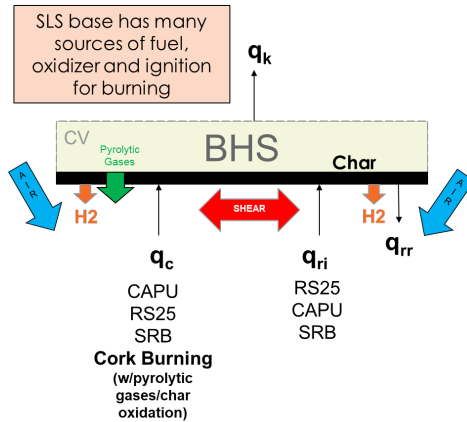


**Figure 34. Schematic of the Core Stage base heat shield's sources of fuel, oxidizer and ignition that can lead to TPS cork combustion;  $q_{ri}$  = incident radiation,  $q_c$  = incident convection;  $q_{rr}$  = reradiation;  $q_k$  = conduction; shear loads further leads to TPS recession and larger influence of cork burning**

## B. Post-Green Run Base Heating Models and AR01 Base Heat Shield Redesign

Equations 16 – 23 detail the methodology in developing post-green run (PGR) base heating models from all the DFI data from GR HF1 and HF2. Equation 16 derives the cork combustion convective heat transfer coefficient from collocated calorimeter, radiometer, gas temperature probe and thermocouple from GR HF2. The calorimeter and radiometer used serial calibration specific to that gauge. Raw counts were outputted from the data files and then serial calibration coefficients were used to obtain accurate engineering units. The radiometer mean value (Equation 17) prior to cork ignition was used since all

radiometers failed upon the large-scale fire regime. It was assumed that the CAPU and RS25 plume-induced radiation did not change due to a large-scale fire regime and it was held constant. It was also confirmed that the cork combustion radiative environment would be small due to the small integrated flame front volume. The incident radiation term is used in these calculations. The wall temperature was the embedded calorimeter temperature measurement. The gas temperature probe records the boundary layer stagnation temperature or recovery temperature based on its design. Equation 18 is the derived equation for cold wall cork combustion convective heating rates from the heat transfer coefficient derived in Equation 1. Equations 19 and 20 are the uncertainty quantification of estimated cold wall convective heating rates. It is a function of temporal, spatial and gauge variabilities. Equation 21 is used to develop a mean + 1 sigma environment. For application to the flight environment, the cork combustion convective heating rates were held constant during the large-scale fire regime. Theoretically, the convective heating rates would decrease as the oxygen availability and density decrease, but such data was not available. There were numerical approaches that were considered to quantify this decrease in convective heating, but it would lead to large uncertainty and schedule was a factor. Equation 22 are updated radiation environments derived from GR HF1. GR HF1 radiation data was used because it was a similar base configuration as flight. Basically, the radiation models were corrected using sea-level GR model comparisons with flight-scale radiation measurements. Equation 23 is the cold wall total heating rates which is a function of the cork combustion cold wall convective heating rates obtained from GR HF2 and the radiative heating rates obtained from the corrected radiation models. Data from both GR hot-fire tests were used to establish updated PGR base heating models.

The other critical component was cork combustion onset and flameout predictions for flight PGR models. Since there was limited data on the onset and flameout, ignition and flameout models could not be derived. To be conservative, we assumed that base heat shield P50 cork ignition would occur upon SRB ignition at T-0 seconds and we assumed that flameout would occur when peak gas recirculation was occurring in the base. The theoretical rationale was that the recirculated plume gases would disable any freestream oxygen from reaching the base heat shield and quench any cork combustion occurring. The cork combustion is quenched at peak base pressure at T+103 seconds as seen in Figure 35.

Figure 36 shows the constant cork combustion convective heating environments developed from the PGR models. Here the first 103 seconds are updated using the PGR model and then it collapses to the standard baseline SPEC model (pre-PGR) which is derived mainly from power-on wind tunnel data (ATA-002) and computational simulations [5]. Figure 37 shows the total heating environment comparisons between the SPEC models and the PGR models for various body points on the base heat shield. As observed both the convective and total heat rates show a large augmentation in heating due to the TPS cork combustion environments. This increases the base heat shield total heat rates by a factor of 2x from the baseline at lift-off and increases to a factor of 4x later in flight which augments the total heat load. Both increases to rate and load lead to large increases in TPS recession rates. It was predicted that cork combustion would occur for the entire base heat shield during ascent and so all body points on the base heat shield were updated by the PGR models as shown in Figure 38. Seven PGR models were then applied to all the body points on the base heat shield. No combustion environments were included on the boat tail or the engine thermal blankets because here cork combustion environments were not observed. Figure 39 shows what environment the bare TPS would experience between GR HF2 and predicted AR01 flight. As can be seen the total heat rates are many factors larger than the SLS-SPEC model early in flight which drives the total heat load and recession rates. For instance, the PGR model derived total heat load is about 165% and 135% greater than the SLS-SPEC model for island 031 and 027 (base center), respectively.

The PGR updated base heating models were provided to both Boeing Thermal and the MSFC Thermal Analysis and Controls Branch for assessment, 12 months prior to Artemis I launch. Both groups conducted a thermal assessment to determine if these much larger heating rates and heat loads early in flight impacted the recession of the heat shield. It was determined that the updated PGR base heating models led to multiple burn throughs within the base heat shield with the baseline TPS configuration. Burn throughs can impact the membrane aluminum structure with direct plume impingement and lead to thermal buckling and deformation of the structure in flight and hot-gas intrusion impacting the TVC controls and propulsion system components. As a result, Boeing decided to increase the Hypalon/P50 cork thickness in regions where the environments were considerably higher. This difference in SLS Core Stage base TPS configuration was compared between the PGR and SPEC models as shown in Figure 40. It can be seen that there was an increase in TPS thickness of 140% for most of the heat shield and 190% increase in TPS

thickness at the manhole cover. This more robust heat shield showed no burn throughs with the updated PGR models through thermal modeling and showed that the metal substrate temperature met requirements from lift-off to Main Engine Cut-Off (MECO). The initial charred base heat shield was removed at the Vehicle Assembly Building and the new and more robust heat shield to account for the updated base heating environments was installed prior to AR01 flight. As a result, an optimal base configuration with much less risk of TPS burn throughs was implemented prior to AR01 launch. This substantially reduced risk to the SLS Program.

$$h_{c,f,TOT027} = \frac{\dot{q}_{t,f,TOT027} - \bar{q}_{r,n,RAD027}}{T_{g,f,GTP027} - T_{w,f,TOT027}} \quad (16)$$

$$\bar{q}_{r,n,RAD027} = \frac{1}{n} \sum_{i=0}^{i=n} \dot{q}_{r,RAD027} \quad (17)$$

$$\dot{q}_{c,f,0F,TOT027} = h_{c,f,TOT027}(T_{g,f,GTP027} - 459.7) \quad (18)$$

$$\sigma_{c,f,0F}^2 = \left( \frac{\partial q_{c,f,0F}}{\partial q_{t,f,0F}} \right)^2 \sigma_{t,f,0F}^2 + \left( \frac{\partial q_{c,f,0F}}{\partial q_{r,f}} \right)^2 \sigma_{r,f}^2 \quad (19)$$

$$1\sigma_{\dot{q}_{c,f,0F}} = \sqrt{\sigma_{t,temp}^2 + \sigma_{t,G}^2 + \sigma_{r,temp}^2 + \sigma_{r,G}^2} \quad (20)$$

$$\bar{q}_{c,f,0F,TOT027} + 1\sigma_{\dot{q}_{c,f,0F}} = \frac{1}{n} \sum_{i=0}^{i=n} \dot{q}_{c,f,0F,TOT027} + 1\sigma_{\dot{q}_{c,f,0F}} \quad (21)$$

$$\dot{q}_{r,GR LL FLT,RS25-CAPU,RAD027} = \left[ \frac{\bar{q}_{r,n,RAD027}}{\bar{q}_{r,n,GR RS25,GASRAD} + \bar{q}_{r,n,GR CAPU,GASRAD}} \right] \dot{q}_{r,FLT,RS25/CAPU,RAD027} \quad (22)$$

$$\dot{q}_{t,GR LL FLT,TOT027} = \bar{q}_{c,f,0F,TOT027} + 1\sigma_{\dot{q}_{c,f,0F}} + 1.25\dot{q}_{r,GR LL FLT,RS25-CAPU,RAD027} + 1.25\dot{q}_{r,FLT,SRB,RAD027} \quad (23)$$

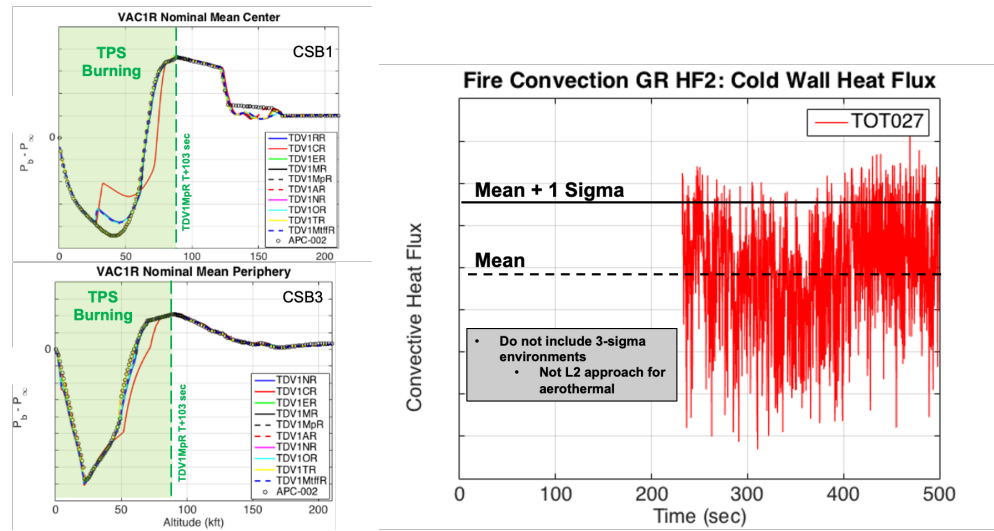


**Figure 35. (left)** base pressure differential vs. altitude which shows the quenching/flame-out altitude and time point; **(right)** cold wall mean and mean + 1 sigma cork combustion convective heating vs. time profile

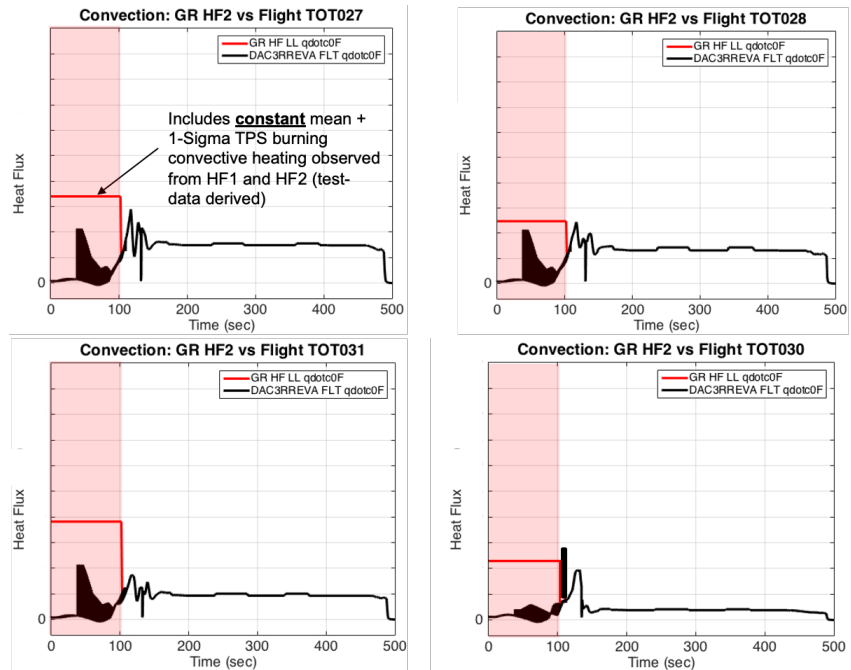


**Figure 36.** PGR vs. SLS-SPEC base convective heating models for: (top-left) TOT027 island, (top-right) TOT028 island, (bottom-left) TOT031 island, (bottom-right) TOT030 island

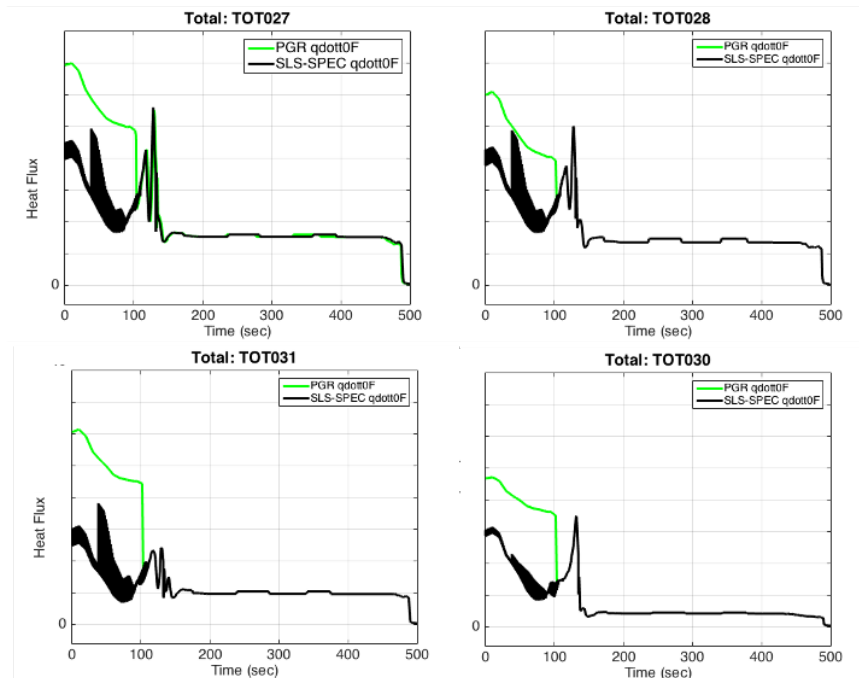


**Figure 37.** PGR vs. SLS-SPEC base total heating models for: (top-left) TOT027 island, (top-right) TOT028 island, (bottom-left) TOT031 island, (bottom-right) TOT030 island

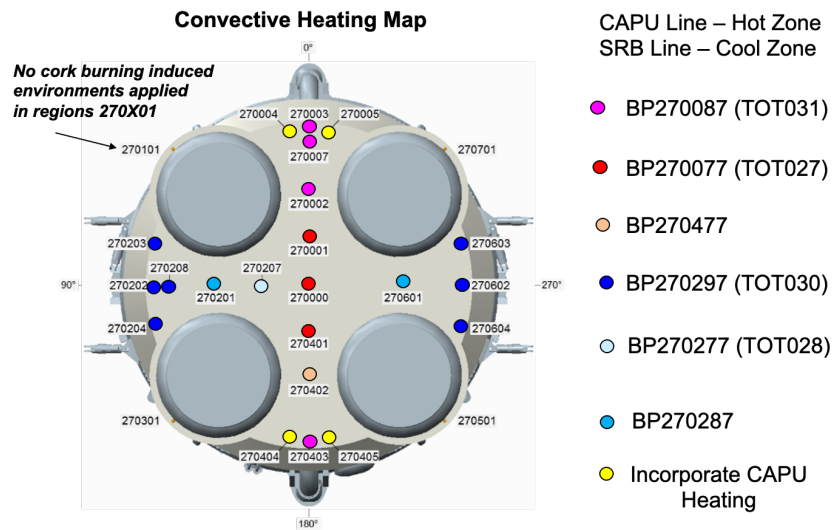


**Figure 38.** Base heating PGR models updated the following body points on the BHS and was delivered to Boeing and NASA Thermal Branches

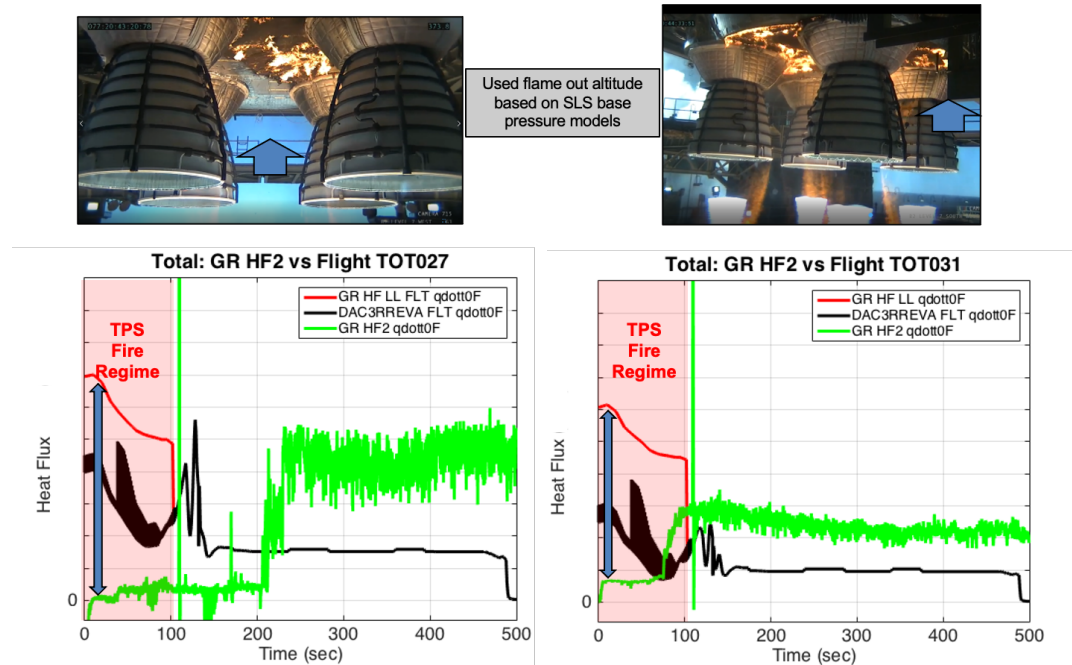


**Figure 39.** Total base heating profiles of the PGR model, SLS-SPEC model and GR HF2 data for DFI island TOT027 (left) and island TOT031 (right); supporting visual imagery data of the cork combustion with a blue arrow showing the approximate locations of the DFI island

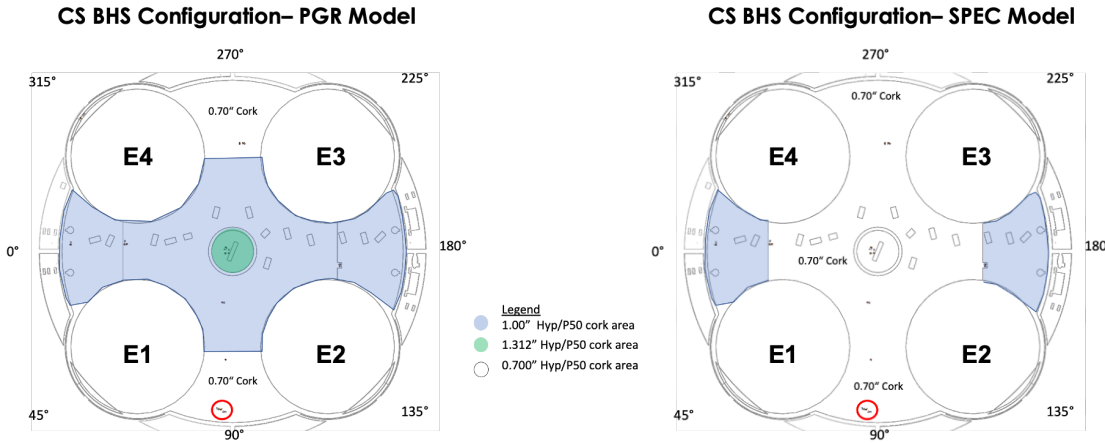


**Figure 40.** (left) Core Stage BHS TPS configuration based on PGR models; this configuration was flown during Artemis I; (right) BHS TPS configuration based on SPEC models

## VI. Conclusions

This comprehensive study investigates the Green Run Core Stage base flow physics and TPS response due to CAPU plume exhausts, CAPU extensions, TPS cork combustion and RS-25 radiative environments. IR and VIS imagery data in conjunction with aerothermal flight sensor data provide us with strong evidence of Hypalon/P50 cork combustion environments, source of anomalies and the effects of the hot CAPU base flow environments. Mitigation analysis was completed in sizing the sacrificial cork TPS on the base heat shield and designing the CAPU extension for GR HF2. Based on our baseline heating models and Green Run flight-scale test data, updated PGR TPS cork combustion convective heating and radiation models were developed for Artemis I flight vehicle. This led to a redesign of the base heat shield one year before launch to prevent a large-scale burn through of the TPS. Here for the first time, base flow physics, TPS response and associated environments for the Core Stage at flight-scales have been investigated.

For Shuttle Orbiter, most of the plume-induced environments were one-way coupled where the plume interacts with the non-catalytic wall TPS. However, observations with GR HF1 and HF2 show that the plume-induced base flow field are two-way coupled with a catalytic wall TPS for the SLS Core Stage. Base flow environments are inherently complex environments with inviscid shock structures, turbulent and

laminar boundary layers, viscous flow structures, different flow regimes as a function of altitude, potential for afterburning and now the potential for two-way coupling between plume-induced environments and TPS material interactions. More research, model development and understanding need to occur in characterizing this two-way coupled base flow phenomena for future SLS flights. Based on PGR models, TPS combustion environments dominate the heat rates and loads early in flight. Historically, base convective heating leads to the highest aerothermal environments on a launch vehicle.

## Acknowledgements

Thanks to the efforts of Mark Hooton, Steve Holmes and Eric Vanderslice (BHS Anomaly Team), the Boeing Aerothermal, Thermal and Flight Sciences Groups (Robin Taylor, Brian Emery, Michael Robinson, Aaron Kirk and Scott Bird) and the technical staff within the Aerosciences Branch (EV33), Thermal Analysis and Controls Branch (Mark Wall and Darrell Davis) and Darrell Gaddy of the Propulsion Thermal Branch at NASA MSFC.

## References

- [1] Mullen, C.R. et al (1972), Saturn Base Heating Handbook, NASA CR-61390, NASA Marshall Space Flight Center, Huntsville, AL.
- [2] Greenwood, T.F., Y. C. Lee, R. L. Bender, and R.E. Carter (1984), "Space Shuttle base heating", *Journal of Spacecraft and Rockets*, Vol. 21, No. 4, pp. 339-345, [doi.org/10.2514/3.25660](https://doi.org/10.2514/3.25660)
- [3] Boeing Integrated Team (1999), Space Shuttle Plume Heating Methodology Report, NASA/Boeing Document No. SSD97D0370, Huntington Beach, CA.
- [4] Mehta, M. (2022), "Launch Vehicle Base Flows", Advanced Modeling and Simulation Seminar, NAS Division, NASA Ames Research Center, Moffet Field, CA.
- [5] Morris, C.I. (2015), "Space Launch System Ascent Aerothermal Environments Methodology", 53rd AIAA Aerospace Sciences Meeting, AIAA SciTech, (AIAA 2015-0561), Kissimmee, FL.
- [6] NASA SLS Core Stage Green Run Test Independent Review – Final Report, Green Run Independent Review Team, NASA Marshall Space Flight Center, Huntsville, 2017.
- [7] MEDTHERM Corporation, "Coaxial Thermocouple Probes", Bulletin 500, MEDTHERM Co, Huntsville, AL, 2000.

- [8] Kurtz, A.D. et al (2003), "Latest ruggedized high temperature piezoresistive transducers", NASA 2003 Propulsion Measurement Sensor Development Workshop, Kulite Semiconductor Products, Inc. Huntsville, AL.
- [9] Nanigian J. and D. Nanigian (2006), "Unique thermocouple to measure the temperatures of squibs, igniters, propellants, and rocket nozzles", Proc. SPIE Paper 6222, Sensors for Propulsion Measurement Applications, 622203, (May 05, 2006).
- [10] Sakraker, I. et al (2021), "Performance of cork-based thermal protection material P50 exposed to air plasma" *CEAS Space Journal*, doi.org/10.1007/s12567-021-00395-z
- [11] Smith, E., B. Lamb, R. Beck and E. Fretter (1992), "Thermal/Ablation Model of Low Density Cork Phenolic for the Titan IV Stage I Engine Thermal Protection System", AIAA 92-2905, Nashville, TN
- [12] Luke, E. A., Tong, X., Wu, J., Tang, L. and Cinnella, P., A Step Towards 'Shape-Shifting' Algorithms: Reacting Flow Simulations Using Generalized Grids, AIAA Paper 2001-0897, Jan. 2001
- [13] White, F.M. Viscous Fluid Flow, McGraw-Hill, Inc., New York: 1991.
- [14] Feikema, D. et al (1991), "Blowout of non-premixed flames: maximum coaxial air velocities achievable, with and without swirl, *Combustion and Flame*, Vol. 86, pp. 347-358.
- [15] Dahm, W.J.A. and A.G. Mayman (1990), "Blowout limits of turbulent jet diffusion flames for arbitrary source conditions" *AIAA Journal*, Vol. 28, Iss. 7.